Neuregulin1 nuclear signaling influences adult hippocampal neurogenesis and regulates a schizophrenia susceptibility gene network within the mouse dentate gyrus.

Prithviraj Rajebhosale[1,7], Alice Jone[2,7], Kory R. Johnson[3], Rohan Hofland[4], Camille Palarpalar[5,8], Samara Khan[5,8], Lorna W. Role[6], David A. Talmage[1]

[1] Genetics of Neuronal Signaling Section, National Institute of Neurological Disorders and Stroke, NIH, Bethesda, MD 20892, USA.
[2] Current Address: Regulatory Affairs Division, STERIS Corporation, Mentor, OH, 44060
[3] Bioinformatics Core, National Institute of Neurological Disorders and Stroke, National Institutes of Health, Bethesda, MD 21042, USA.
[4] Current Address: MSTP, Albert Einstein College of Medicine, Bronx, NY 10461.
[5] Previous Address: Undergraduate Biology, Stony Brook University, Stony Brook NY 11794.
[6] Laboratory of Circuits, Synapses, and Molecular Signaling, National Institute of Neurological Disorders and Stroke, NIH, Bethesda, MD 20892, USA.
[7] Co-first authors.
[8] These authors contributed equally.

Corresponding Author: David Talmage (David.Talmage@nih.gov)

Abbr. Title: Regulation of gene expression and neurogenesis by Nrg1 nuclear signaling.

Number of pages: 66, **Number of figures**: 6, **Number of supp.figures**: 10, **Number of supp. tables**: 7, **Number of words**: Abstract (303), Introduction (454), Discussion (1782).

DISCLOSURES

The authors have no conflicts of interest to declare.

A version of this manuscript has been posted as a preprint on bioRxiv: https://doi.org/10.1101/2022.08.10.503469

ACKNOWLEDGEMENTS

This work was supported by the Intramural Research Program of NINDS and by MH087473 (to DAT). We would like to thank Dr. Shaoyu Ge (Stony Brook University, NY) and Dr. Mala Ananth (NINDS) for valuable discussions. We would also like to thank Dr. Abdel Elkahloun and Bayu Sisay (NHGRI sequencing core facility) for providing NGS consultation and services and the NINDS Light Imaging Facility. Finally, we would like to thank Wendy Akmentin, Taylor Muir and Li Bai for expert technical assistance in data curation. Artwork/Schematics were created with BioRender.com.

ABSTRACT

Neuregulin1 (NRG1) signaling is critical for aspects of neuronal development and function from fate specification to synaptic plasticity. Homozygous *Type III Nrg1* deletion (the predominantly neuronally expressed isoform of *Nrg1*) is lethal, and although heterozygous mice survive, they show several central and peripheral neurodevelopmental defects [1]. TYPEIII NRG1 is a synaptic protein which engages in bi-directional signaling with its receptor ERBB4. Forward signaling engages ERBB4 phosphorylation and downstream signaling, whereas back signaling engages two known mechanisms: 1. local axonal PI3K-AKT signaling in the cell expressing NRG1 and 2. cleavage by gamma secretase resulting in cytosolic release of the intracellular domain (ICD), which can traffic to the nucleus [2, 3]. To dissect the contribution of these alternate signaling strategies to neuronal development we generated a transgenic mouse with a missense mutation ($V_{321}L$) in the Nrg1 transmembrane domain that disrupts nuclear back signaling with minimal effects on forward signaling or local back-signaling. We combined RNA sequencing, cell-type composition analysis using immunohistochemistry, retroviral fate mapping of neural stem cells and various network analyses of transcriptomic data to investigate the effect of disrupting NRG1 nuclear back-signaling in the mouse dentate gyrus (DG).

The $V_{321}L$ mutation impairs ERBB4-induced nuclear translocation of the NRG1 ICD. Differentially expressed genes (DEGs) between wild-type (WT) and $V_{321}L$ mice predicted dysregulation of cell cycle regulation, differentiation, neurogenesis, and dendritic growth in the mutant DG. We confirmed that $V_{321}L$ mice show reduced neural stem cell (NSC) proliferation, altered cell cycle dynamics, altered fate specification of NSCs, and dendritic dysmorphogenesis. Known schizophrenia (SCZ)-susceptibility genes were dysregulated in the $V_{321}L$ DG. These genes coordinated a larger network with other dysregulated genes. WGCNA and protein-interaction network analyses revealed striking similarity between DG transcriptomes of $V_{321}L$ mouse and humans with schizophrenia. Comparison of $V_{321}L$ mouse and human schizophrenia DG transcriptomes showed shared alterations to ribostasis, proteostasis, and mitostasis.

SIGNIFICANCE STATEMENT

Gene x environment interactions are a significant component of psychiatric disorders. While considerable progress has been made in uncovering genetic variation associated with psychiatric disorders, an understanding of how environmental influences interact with disease-associated variation has remained elusive. Here we show that a schizophrenia-associated mutation in the NRG1 gene disrupts the protein's ability to communicate extracellular signals to the neuronal genome which results in altered expression of a gene network enriched for schizophrenia-susceptibility genes. Given the synaptic localization of NRG1 and its receptor ERBB4, synaptic contact is predicted to be a regulator of the generation of nuclear signaling by NRG1. Thus, our data provide a conceptual framework for future studies to integrate environmental risk factors influencing synaptogenesis and regulatory genetic variation associated with disease.

INTRODUCTION

The Neuregulin 1 (NRG1)-ERBB4 signaling axis is an important regulator of synapse formation and function throughout the nervous system [4-6]. TYPE III NRG1, located pre-synaptically, participates in bidirectional signaling i.e., acting as both a ligand and a receptor for ERBB4 [2, 7]. Upon binding ERBB4, the TYPEIII NRG1 C-terminal intracellular domain (ICD) can be liberated from the membrane by an intramembrane proteolytic event mediated by the gamma secretase enzyme complex. Following this cleavage, the ICD translocates to the nucleus where it can function as a transcriptional regulator (nuclear back signaling) [2]. Additionally, binding of ERBB4 can also induce local activation of PI3K-AKT signaling [3]. Thus, activation of TYPE III NRG1 by ERBB4 can induce two distinct modes of signaling. Cortical neurons cultured from *Type III Nrg1* KO mice show deficits in axonal and dendritic outgrowth and branching, which were rescued by re-expression of full-length TYPE III NRG1 protein [8]. However, nuclear back signaling defective forms of TYPE III NRG1, lacking the nuclear localization sequence (NLS) or mutations in the gamma secretase cleavage site,

were only able to rescue axonal growth and not dendritic growth [8]. In line with this, TYPE III NRG1 hypomorphic mice show reduced hippocampal dendritic spine density and overexpression of the nuclear NRG1 ICD results in increased dendritic spine density in cultured hippocampal neurons, whereas overexpression of NRG1 ICD lacking the NLS did not [8, 9]. *Type III Nrg1* heterozygous mice also show other endophenotypes of schizophrenia such as pre-pulse inhibition deficits, increased ventricle volume, altered hippocampal activity and connectivity [8, 10, 11].

A missense mutation in *NRG1* resulting in a single amino acid substitution in a transmembrane valine (to leucine; rs74942016- results in Val→Leu at position 321 in TYPEIII NRG1 β1A) was found to be associated with schizophrenia (and more strongly with psychosis) in a Costa Rican population [12]. Intriguingly, gamma secretase cleaves between cysteine 320 and valine 321, and leucine substitution for V_{321} results in impaired cleavage and reduced nuclear translocation of the ICD [8, 13]. This presents the intriguing possibility that loss of a specific signaling modality within this multifunctional protein might contribute to some features of neurodevelopmental disorders such as schizophrenia.

To isolate the effects of nuclear back-signaling by the NRG1 ICD on neuronal development and transcriptomic regulation we generated transgenic mice harboring the $V_{321}L$ mutation in NRG1. The dentate gyrus (DG) serves as the gate for incoming information into the hippocampus, and neuronal development is an ongoing process in the DG, owing to the presence of a neurogenic niche in the postnatal brain, thereby allowing is to broadly sample effects on various stages of neuronal development. Thus, we chose the DG as a candidate region to begin investigating the effects of impaired gamma-secretase processing of NRG1.

RESULTS

Generation of the *Nrg1* $V_{321}L$ mutant mouse to study γ-secretase-mediated NRG1 signaling.

To examine the effect of the $V_{321}L$ substitution on TYPE III NRG1 signaling, we generated a knock-in germline mutation in mice. The $V_{321}L$ mutation (gtg→ttg) was introduced into C57Bl6 embryonic stem cells using a bacterial artificial chromosome (BAC) construct (**Figures 1A-D**). Heterozygotes were interbred, and offspring were born at the expected Mendelian ratios (**Figure 1E**). Homozygous $V_{321}L$ mutants were viable and

fertile, with no outward morphological or growth abnormalities. Homozygous animals were able to interbreed and yielded normal-sized litters with offspring that appeared healthy. The $V_{321}L$ mutation was also viable on a TYPE III NRG1 knock-down background, as a *Nrg1*$^{L/L}$ x Type III *Nrg1*$^{+/-}$ cross yielded both *Nrg1*$^{V/L}$ and *Nrg1*$^{L/-}$ offspring.

$V_{321}L$ mutation in NRG1 impairs gamma-secretase mediated cleavage in vitro [13]. We performed subcellular fractionation to isolate nuclei from cortical and hippocampal homogenates of $V_{321}L$ homozygous mutant and their wildtype (WT) litter- and cage-mates and compared the levels of NRG1 ICD by immunoblot analysis (using the sc-348 NRG1 antibody) (**Figure 1-1A**). Nuclei isolated from $V_{321}L$ animals showed lower levels of NRG1 ICD compared to nuclei from wildtype counterparts, consistent with diminished NRG1 nuclear signaling in the mutant cortex and hippocampus.

TYPE III NRG1 back-signaling results in the appearance of distinct clusters of the ICD in the nucleus [2]. To determine whether nuclear ICD clusters were altered in neurons from $V_{321}L$ mice, we cultured dispersed hippocampal neurons from postnatal day 4 (PND 4) WT and $V_{321}L$ mice (culture age:17 days *in vitro* (DIV)). To assess the composition of our cultured hippocampal neurons, we immunostained for the DG marker PROX1 along with βIII TUBULIN (TuJ) to identify all neurons (**Figure 1-1B**). We found ~70% of the neurons were dentate granule cells (GCs) (Median: 69.1% ± 0.02% std. dev). We stimulated these cultures with soluble recombinant ectodomain of ERBB4 (sB4) and quantified nuclear ICD clusters (**Figure 1-1C left**). We found that stimulation with sB4 increased the number of nuclear ICD clusters in neurons from WT mice (**Figure 1-1C right;** WT Veh v. WT sB4 One-way ANOVA Bonferroni adj. $p<0.0001$). This increase in nuclear ICD clusters was blocked by pre-treatment with the γ-secretase inhibitor, DAPT (**Figure 1-1right;** WT Veh v. WT (sB4) + DAPT Bonferroni adj. $p>0.9999$). We did not observe increased ICD clusters in neurons from $V_{321}L$ mice treated with sB4 (**Figure 1-1C right;** $V_{321}L$ Veh v. $V_{321}L$ (sB4) Bonferroni adj. $p>0.9999$). There was no difference in nuclear clusters at baseline between WT and $V_{321}L$ neurons (WT Veh v. $V_{321}L$ Veh Bonferroni adj. $p>0.9999$).

Type III Nrg1 back-signaling operates via two known mechanisms – 1. Local axonal, PI3K signaling and 2. γ-secretase-dependent nuclear signaling, required for dendritic growth and complexity. We asked whether

neurons from $V_{321}L$ mice are selectively deficient in dendrite development in response to ErbB4 stimulation. Cortical neurons from embryonic (E18.5) WT and $V_{321}L$ mouse pups were cultured for 3 days *in vitro*. On the third day, neurons were treated with sErbB4 with or without pharmacological inhibition of PI3K using Wortmannin (WM) or γ-secretase using L-685,458 (L6).

Neurons from WT mice showed increases in axonal and dendritic length in response to ErbB4 treatment which were blocked by WM and L6 respectively (**Figure 1-2A and 1-2B dark blue boxes**; axonal length: WT NT v. WT B4 $p=0.0002$; dendritic length: WT NT v. WT B4 $p=0.0019$). WM treatment did not block ErbB4-induced dendritic growth and L6 treatment did not prevent ErbB4-induced axonal growth (axonal length: WT L6 v. WT L6+B4 $p<0.0001$; dendritic length: WT WM v. WT WM+B4 $p<0.0001$). These results agree with previously published data showing that Nrg1 nuclear back-signaling influences dendritic growth [8]. These data also establish that stimulation of axonal growth requires PI3K signaling and that these two modes of Nrg1 back signaling are independent.

Neurons from $V_{321}L$ mice showed increased axonal length in response to ErbB4 stimulation which was blocked by WM treatment and not by L6 (**Figure 1-2A light blue boxes**; axonal length: $V_{321}L$ NT v. $V_{321}L$ B4 $p=0.0014$, $V_{321}L$ WM v. $V_{321}L$ WM+B4 $p=0.1113$, $V_{321}L$ L6 v. $V_{321}L$ L6+B4 $p=0.0289$). On the other hand, $V_{321}L$ neurons did not show increases in dendritic length in response to ErbB4 stimulation (**Figure 1-2B** dendrite length: $V_{321}L$ NT v. $V_{321}L$ B4 $p>0.9999$). These results indicated that PI3K signaling-dependent axonal growth was intact in $V_{321}L$ mutant mice with a selective disruption of γ-secretase-dependent dendritic growth.

Thus, $V_{321}L$ mice show disruptions to intramembrane proteolysis of Nrg1 and thereby to nuclear translocation of the ICD. Additionally, we demonstrate that dendritic growth in response to ERBB4 stimulation was absent in neurons from $V_{321}L$ mutant mice whereas axonal growth in response to ERBB4 was intact.

Changes in NRG1 $V_{321}L$ mutant dentate gyrus transcriptome point to aberrant neurogenesis, cell cycle dynamics, and dendrite development.

The NRG1 ICD has strong transactivation properties [2]. $V_{321}L$ mice have impaired nuclear translocation of the ICD (**Figure 1-1**). Thus, we predicted that impaired nuclear signaling by the NRG1 ICD would result in transcriptomic changes.

We extracted RNA from microdissected DG from WT and $V_{321}L$ mice for RNA sequencing (**Figure 2A**). Differential gene expression analysis revealed 1312 significantly dysregulated genes (colored dots, ANCOVA corrected p≤0.1 and linear fold change of ±1.25) between WT and $V_{321}L$ mice (**Figure 2B; Table 2-1**). We found that the DG-specifying transcription factor *Prox1* and mature granule cell marker *Calb1* were both downregulated. To confirm this, we performed immunohistochemistry (IHC) on WT and $V_{321}L$ DG brain sections and quantified PROX1 and CALB1 protein expression in the granule cell layer of the dorsal DG (**Figure 2C**). PROX1 and CALB1 expression were significantly lower in the $V_{321}L$ DG compared to WT (**Figure 2C right**, PROX1: WT v. $V_{321}L$ p=0.029 Mann-Whitney Rank Sum Test, U=0; CALB1: WT v. $V_{321}L$ p=0.029 Mann-Whitney Rank Sum Test, U=0).

To identify possible functional alterations that might result from transcriptional dysregulation in $V_{321}L$ mice, we used ingenuity pathway analysis (IPA) to find cellular processes regulated by the significantly dysregulated genes. Several functions along the neurodevelopmental trajectory were predicted to be disrupted in the $V_{321}L$ DG, including cell proliferation, differentiation, and dendrite development (**Figure 2D; Table 2-2**). In line with this we noted downregulation of *Dock10*, which encodes a Rho guanine exchange factor enriched in the dendritic spines of DG GCs [16, 17] and of *Synpr*, which encodes for a synaptic vesicle protein enriched in DG GC axons [18]. We performed IHC for DOCK10 and SYNPR in WT and $V_{321}L$ brain sections and quantified expression of these proteins in the molecular layer (GC dendrites) and CA3 (GC axons) respectively (**Figure 2-1A**). DOCK10 expression was significantly lower in $V_{321}L$ molecular layer compared to WT (**Figure 2-1B**, WT v. $V_{321}L$ p=0.0286 Mann-Whitney Rank Sum Test, U=0). We did not find a change in overall level of SYNPR protein level by IHC however, the overall area of the SYNPR+ mossy fibers was significantly lower in $V_{321}L$ DG (**Figure 2-1C**, p=0.0286 Mann-Whitney Rank Sum Test, U=0). Additionally, we noted a subtle difference in the targeting of CA3 by the mossy fibers in the $V_{321}L$ DG. Mossy fibers projecting through the suprapyramidal tract preferentially innervate the stratum lucidum (Slu) where they synapse onto proximal apical dendrites of CA3 pyramidal neurons [19]. The ratio of the SYNPR immunoreactivity in the Slu to the CA3 pyramidal cell layer (Pyr) was lower in $V_{321}L$ DG compared to WT, albeit this did not reach our criterion for statistical significance (**Figure 2-1D**, p=0.0571).

Disease annotations in IPA indicated that dysregulated genes in the $V_{321}L$ DG were enriched in schizophrenia-susceptibility genes, indicating that the $V_{321}L$ mutation alters the transcriptional landscape in ways that have been associated with the genetic architecture of schizophrenia (**Figure 2E**). We also found that dysregulated genes in $V_{321}L$ mice were enriched in cancer-associated genes, consistent with predicted changes in regulation of cell proliferation (**Table 2-3**).

We next asked whether the differentially expressed genes shared transcriptional regulatory mechanisms. [20-23]. We identified that the 664 significantly upregulated genes in $V_{321}L$ mice were enriched for genes predicted to be regulated by members of the polycomb repressor complex 2 (PRC2) (SUZ12, EZH2), RE1-Silencing Transcription factor (REST), and the CTCF-cohesin complex (CTCF, RAD21, SMC3) involved in chromatin looping. We grouped these regulators into two higher order groups: 1. PRC2+REST and 2. CTCF-Cohesin (**Figure 2-2B**). We found that 126 of the 664 upregulated genes were targets for regulation by the PRC2 and 81 of the 664 upregulated genes were targets of REST; 28 of these 81 REST-target genes (~35%) were also targets of the PRC2. Gene ontology analyses for the PRC2-target genes revealed that genes predicted to be involved in synapse assembly, synaptic transmission, and neuronal differentiation were enriched in this group (**Figure S4B, Top; Table 2-4**). The CTCF-Cohesin regulated genes were enriched for functions such as axon guidance, cell migration, synapse assembly, and protein phosphorylation (**Figure 2-2B, Bottom; Table 2-4**). Intriguingly, we found that EZH2 and EED (catalytic subunits of PRC2) were downregulated in the RNASeq comparison between WT and $V_{321}L$ DG (**Table 2-1**).

The 647 downregulated genes showed strongest enrichment of genes predicted to be regulated by the transcription factor E2F4 (odds ratio: 3), Upstream Binding Transcription Factor (UBTF), Sin3 Transcription Regulator Family Member A (SIN3A), and Myc-associated Factor X (MAX) (**Figure 2-2C**). The E2F4-target genes were found to be involved in mitotic spindle organization, microtubule organization, RNA-splicing, and DNA replication (**Figure 2-2C**). Overall, the downregulated genes were found to be involved in positive regulation of mitosis.

The observed changes in gene expression strongly implicate the NRG1 ICD as a regulator of E2F4 and PRC2 function during a neurodevelopmental program. Based on these data we predicted that there would be altered proliferation and neural differentiation within the $V_{321}L$ mutant neurogenic niche.

Abnormal progenitor pool maintenance and differentiation in the $V_{321}L$ mutant dentate gyrus

TYPE III NRG1 mRNA (**Figure 3-1A**) and protein (**Figure 3-1B**) were widely expressed within the DG, particularly within the subgranular zone (SGZ) and the granule cell layer (GCL). In the neurogenic niche, TYPE III NRG1 immunoreactivity was observed in cells located on the border of the hilus and the granule cell layer (**Figure 3-1B right; inset**). To determine if TYPE III NRG1 was expressed in neural progenitors in the DG, we labelled cells undergoing DNA synthesis with the thymidine analogue EdU [24, 25] and stained brain sections for TYPE III NRG1 24 hrs later. Subsets of EdU-positive cells in the dentate gyrus expressed TYPE III NRG1 (**Figure 3-1C**). We also stained sections for doublecortin (DCX), a marker for neuroblasts and immature neurons, and TYPE III NRG1. Some, but not all DCX-positive cells expressed TYPE III NRG1 (**Figure 3-1D**). Therefore, TYPE III NRG1 is expressed in proliferative neural stem cells, immature and mature neurons of the adult mouse dentate gyrus.

We next quantified the effect of the $V_{321}L$ mutation on neurogenesis in the hippocampus (**Figure 3A & 3B**). Stereological analysis revealed a statistically significant decrease in the proliferative population (Ki67+) in $V_{321}L$ animals compared to WT (**Figure 3A**; $p= 0.0271$, Welch's t-test), whereas newborn neuron (DCX+) production was comparable between $V_{321}L$ and WT animals **Figure 3B** ($p=0.9865$, Welch's t-test). Thus, proliferation was stunted in the $V_{321}L$ DG, but this impairment did not result in a difference in the number of newborn neurons produced.

The discrepancy between decreased proliferation and unchanged neuronal production in the $V_{321}L$ DG could be explained by disruptions to the balance between self-renewal maintenance and postmitotic neuronal differentiation, both of which are processes predicted to be disrupted by the $V_{321}L$ mutation based on the transcriptomic data (**Figure 2D)**. Therefore, we asked whether cell cycle dynamics and/or fate commitment by neural stem cells are abnormal in the $V_{321}L$ DG.

To measure the rate of cell cycle reentry, cells in S phase of the cell cycle were first labelled by systemic EdU injection. 24 hours after EdU injection, we collected brain sections and stained them for Ki67 expression. We calculated the overall rate of cell cycle reentry as the proportion of total EdU+ cells that were also Ki67+. We observed a statistically significant decrease in cell cycle re-entry in the $V_{321}L$ DG compared to WT DG (**Figure 3C**; p= 0.0043, Mann-Whitney Rank Sum Test). Therefore, the self-renewing pool of neural progenitors was depleted faster, generating more postmitotic cells in the $V_{321}L$ mutant dentate gyrus.

Given the higher rate of cell cycle exit in $V_{321}L$ DG, we asked if fate programming was affected. $V_{321}L$ and WT DGs were stereotaxically injected with a replication-deficient retrovirus encoding GFP, which only stably infects cell during mitosis. After 14 days, brains were collected for identification of GFP+ progeny. The identity of GFP+ cells were determined by a combination of morphology, DCX immunoreactivity, and Nissl staining. Neural progenitors were identified by short, tangential processes and the lack of radially oriented processes, with or without DCX immunoreactivity (**Figure 3D**, open arrowheads). Immature GCs (iGC) were identified by their radially oriented neurites and DCX+ Nissl+ staining (**Figure 3D**, closed arrowheads). Astrocytes were identified by their star-like morphology, extensive branch ramifications, and lack of DCX immunoreactivity and Nissl staining (**Figure 3D**, yellow arrows).

The results revealed a decrease in the proportion of neural progenitors in the $V_{321}L$ DG compared to WT DG (**Figure 3D**; Two-way ANOVA Genotype x Cell Fate p=0.0003 F (3, 20) =9.864. NP, WT v. $V_{321}L$ Bonferroni-corrected p=0.0026), consistent with the observed depletion of the proliferative pool (**Figure 3A**) and increased rate of cell cycle exit (**Figure 3C**). Interestingly, fate commitment in the $V_{321}L$ DG was disproportionately biased towards the neuronal fate program compared to astroglial fate (**Figure 3D**; iGC, WT v. $V_{321}L$ Bonferroni-corrected p=0.0069). In fact, the proportion of astrocytes generated by the $V_{321}L$ neural stem cells was not significantly different between $V_{321}L$ and WT DG (Astrocyte, WT v. $V_{321}L$ p>0.9999). Additionally, 1-month EdU pulse-chase experiments suggest that survival of neural progenitors and newborn neurons was modestly increased in $V_{321}L$ DG (**Figure 3-2**).

Thus, we found depletion of the proliferative neural stem cell pool, increased cell cycle exit, and disproportionate production of neurons over astrocytes in the $V_{321}L$ DG in agreement with predictions from our

transcriptomic analyses (**Figure 2**). These findings point to an essential role for NRG1 ICD nuclear signaling in neural stem cell maintenance and fate commitment in the adult DG.

The NRG1 $V_{321}L$ mutation compromises maturation of granule cells in the dentate gyrus.

NRG1 nuclear back-signaling is important for neuronal development, playing a cell-autonomous role in dendrite arborization and spine production [9, 26]. Our RNASeq analysis of the $V_{321}L$ DG showed dysregulation of genes involved in dendrite development (**Figure 2D**). Therefore, we examined the dendrite morphology of newborn dentate GCs.

Qualitative observations from DCX immunohistochemistry revealed decreased dendritic complexity of adult-born immature neurons in $V_{321}L$ DG. DCX immunostaining also tended to be weaker in the mutant molecular layer, into which the granule cells extend their dendrites (**Figure 4A, right insets**).

To systematically quantify granule cell dendritic arbors, we used Golgi impregnation to visualize neuronal morphology and only analyzed dendrites of neurons with typical granule cell morphologies (see methods for details on criteria). **Figure 4B** shows two representative tracings of granule cells from each genotype. Total dendritic length was modestly greater in $V_{321}L$ mice, although this difference was not statistically significant (**Figure 4-1A**). Sholl analysis revealed significant increases in $V_{321}L$ dendritic length proximal to the soma (**Figure 4C**; at 80µm away from soma Bonferroni-corrected p=0.052, Two-way RM ANOVA with a significant (Genotype x Distance from soma) interaction p=0.0347).

Dendrite complexity appeared to be compromised in GCs sampled from $V_{321}L$ DGs. In WT neurons most of the dendritic length was distributed in 4th and 5th order, whereas in $V_{321}L$ GCs, the peak of dendritic length was found in 4th order branches with less length distributed in 5th order branches (data not shown). In fact, there was a statistically significant decrease in the proportion of GCs that possessed 5th order branching in $V_{321}L$ GCs, and while a small percentage of WT GCs possessed 6th and 7th order branches, these high order branches were not observed in $V_{321}L$ GCs (**Figure 4D**, 5th order: p= 0.0131, 6th order: p= 0.0815, 7th order: p= 0.458, Fisher's exact test). Total dendritic length and number of branch points were not significantly altered in the $V_{321}L$ DG (**Figure 4-1**).

Altogether, examination of dentate GCs revealed alterations in the dendrites in both mature and immature $V_{321}L$ GCs, especially in distal dendrites. Thus, diminished NRG1 nuclear back-signaling results in persistent and cumulative effects on dendrite growth and complexity across development.

Dysregulation of a functionally connected schizophrenia susceptibility gene network in the $V_{321}L$ DG.

Transcriptomic enrichment analyses combined with empirical studies (**Figures 2,3, and 4**) strongly implicated the NRG1 ICD in regulating a functionally connected network of genes involved in neuronal development (**Figure 2-2**). The enrichment of schizophrenia-associated genes within the dysregulated genes in the $V_{321}L$ DG raised the possibility that the schizophrenia-associated genes might also function within this larger network of genes regulating neuronal development. To gain further insight into how schizophrenia-associated DEGs in the $V_{321}L$ DG, might regulate neuronal development, we first asked if the schizophrenia-associated DEGs functionally interact with a larger set of the DEGs. To do this, we created a merged list of dysregulated genes in the $V_{321}L$ DG whose human orthologs are associated with psychosis, schizophrenia, sporadic schizophrenia, or schizoaffective disorder, under the umbrella term of "schizophrenia spectrum disorders" (SCZ) yielding a total of 67 genes (**Figure 5A;** enrichment p value =5e-7; **Table 5-1**). We then grew a network (see methods) by providing the dataset of the significantly DEGs in the $V_{321}L$ DG seeking to find genes in our dataset that have not been explicitly identified as schizophrenia-associated but might have direct functional interactions with dysregulated schizophrenia-annotated genes. This resulted in a network with 322 nodes and 371 edges, which we called the "SCZ+" network. 49 of the 67 SCZ genes were incorporated into SCZ+ network. (**Figure 5B, right. Table 5-2**). Thus, the bulk (73%) of the schizophrenia-associated DEGs do interact within a larger network of DEGs. Next, we analyzed the topological properties of this network to derive further insight into the nature of these interactions aiming to further distill the role SCZ genes might play within this network.

Analysis of the expanded schizophrenia-susceptibility network (SCZ+) implicated a "hub and spoke" topology. Hub nodes interacted preferentially with a few other nodes as opposed to with each other (i.e. the degree of a node and its topological coefficient were inversely related) (data not shown). We identified 10 hub

nodes using mean clique clustering (MCC), 9 of 10 hubs were part of the primary schizophrenia-susceptibility network (**Figure 5C**). The 10 hubs shared no edges with each other thereby creating 10 distinct modules (red (higher rank) to yellow (lower rank) MCC Top10 nodes). We visualized the first-degree neighbors of these hub genes and found that each of the hub genes coordinated its own mini network as predicted from the network topology (**Figure 5C**). To validate the status of the hub genes as hubs within the SCZ+ network, we reconstructed the SCZ+ network shown in Fig. 5A after removing the hub genes from the network. Exclusion of these 10 hub genes resulted in fragmentation of the network indicated by the drastic increase in the number of components and decrease in the number of edges (**Figure 5D**). Thus, the SCZ genes not only interact with a larger network of dysregulated genes, but a subset of them (9 out of the original 67) play key roles in organizing the network.

To understand the functional link that SCZ genes provide to integrate the SCZ+ network, we performed Gene Ontology analyses on the 49 SCZ genes and the 271 DEGs that became part of SCZ+ network. The SCZ genes were enriched for functions related to synaptic transmission (adj.p=4.02e-8) and were enriched for genes whose products are localized to synaptic membranes (SynGO- adj.p<0.01). Intriguingly, none of the hub genes (90% of which were part of the original schizophrenia-associated gene list) were associated with synaptic transmission. The 271 DEGs that comprised the SCZ+ network were enriched for the annotation-transcriptional regulation (adj.p=0.02) (driven by 52 of the 271 genes) and were enriched for genes whose products are localized to the nucleus (adj.p=0.00002) (**Table 5-3**). These data show that while schizophrenia associated DEGs are enriched for genes involved in synaptic function, hubs that embed these core genes into cellular signaling networks are not obvious mediators of synaptic function.

NRG1 nuclear back-signaling regulates functionally related gene modules.

Transcriptional regulator (TR) analysis showed that DEGs in the $V_{321}L$ DG can be regulated by a small set of transcriptional regulators (e.g. REST, PRC2, E2F4, etc.). TR analysis also showed that DEGs regulated by the same regulators were functionally related (**Figure 2-2**). This result raises the possibility that the NRG1 ICD transcriptionally regulates functionally related genes. To investigate this, we performed weighted gene correlation network analysis (WGCNA) to identify gene co-expression modules associated with the $V_{321}L$

mutation (**Figure 6-1A-C; See supplemental text for details on WGCNA associated with Figures 6-1 and 6-2**). Genes clustered within a WGCNA module have been shown to be functionally related [27]. Thus, we asked whether the genes with correlated expression in each module encode proteins that have functional interactions. We accomplished this using the STRING protein-protein interaction (PPI) database [28] to build PPI networks from the WGCNA modules. Using stringent criteria (see methods) we extracted a PPI network using genes within the WGCNA modules (**Figure 6**). We found that the protein products of genes within the WGCNA modules had highly significant functional interactions forming densely interconnected networks (**Figure 6A, mouseUP module**: 1136 nodes, average node degree=8.2, PPI enrichment p value= 3.56e-13; **Figure 6B, mouseDOWN module**: 712 nodes, average node degree=15, PPI enrichment p value < 1.0e-16.).

To gain insight into the nature of these functional interactions, we analyzed the networks as undirected graphs (**Figure 6**). We identified hub nodes based on their maximal clique centrality (MCC) [29]. The highest MCC ranked genes in the mouseUP and mouseDOWN modules were members of ubiquitin ligase complexes indicating that a functionally related group of hub genes was disrupted within these modules (**Figure 6E**). To probe the significance of these hub genes in maintaining integrity of the larger network and validate their hub status, we removed them from the network and reanalyzed the remaining genes for interactions in STRING for both mouseUP and mouseDOWN modules. Deletion of the MCC hub genes resulted in reduced connectivity within the network and disintegration of the network (**Table 6-1**) thereby supporting their role as hub genes; the hub deleted network resulted in loss of almost all the highest differentially expressed genes between $V_{321}L$ and WT DG as evidenced by the loss of darker colored nodes from the networks (**Figure 6-3 A&B**).

Thus, WGCNA revealed that loss of NRG1 nuclear back signaling results in highly correlated dysregulation of functionally related modules of genes. We noted that there was upregulation of a gene network involved in axonal synapse organization predicted to be regulated by the PRC2 (**Figures 6-1F & 6-1G**); components of the PRC2 were downregulated (**Figure 6-1G; Table 2-1**).

Molecular changes in the mouse $V_{321}L$ mutant DG show similarity with those observed in DG samples from humans with schizophrenia.

The bulk of the genetic variation associated with schizophrenia is regulatory in nature (eQTLs) [30]. However, available databases do not yet provide clear mechanisms for how these variants might influence biological processes that underlie schizophrenia pathology. Our network analyses and ontology analyses on the $V_{321}L$ mouse DG transcriptome allowed us to uncover latent regulatory structure within the transcriptomic data. We next sought to apply the same network analysis pipeline to anatomically matched human DG transcriptomic data from people with schizophrenia to ask which, if any, features uncovered in the analysis of the $V_{321}L$ mouse DG might be represented in human pathology.

We performed WGCNA using published RNASeq data from microdissected DG granule cell layer from healthy controls and people with schizophrenia (93 controls and 75 schizophrenia subjects: 119 males and 49 females) [31] (**Figure 6-2; supplemental text**).

To validate that the WGCNA modules represented functionally interacting components we constructed PPI networks from them (**Figure 6**). We found that the protein products of genes that were part of the human WGCNA modules had highly significant functional interactions (**Figure 6C, humanUP module**: 489 nodes, average node degree= 8.96, PPI enrichment p value= 1.96e-7. **Figure 6D, humanDOWN module**: 1180 nodes, average node degree= 23.56, PPI enrichment p value= <1.0e-16). Similar to the mouse hub gene analysis, the highest ranked hub genes formed networks that are part of ubiquitin ligase complexes (**Figure 6E**).

We created hub networks by selecting the first-degree neighbors for the mouse and human hub genes and asked what biological processes were enriched in these core networks (**Figure 6F**). We found a striking 100% overlap between the mouse and human hub network functions. The mouse and human UP hub networks were enriched for genes involved in synaptic transmission and neurotransmitter receptor regulation by synaptic proteins (**Figure 6F, Top**). The mouse and human DOWN hub networks were enriched for genes involved in several cellular homeostatic functions such as proteostasis, ribostasis, and mitostasis (**Figure 6F, Bottom**).

Thus, these data reveal evolutionarily conserved regulatory programs that can regulate expression of genes that underlie cellular pathology in psychotic disorders.

DISCUSSION

We investigated the cellular and molecular consequences of loss of NRG1 nuclear back signaling due to the $V_{321}L$ mutation (homozygous frequency in human population = 0.002). The $V_{321}L$ mutant mouse model allowed us to probe the consequence of a single genetic change on the transcriptome and neuronal development. This mutation is predicted to alter a specific mode of NRG1 signaling involving membrane (synapse) to nucleus signaling by the NRG1 ICD.

In this study we confirm that loss of nuclear back signaling by the NRG1 ICD in the $V_{321}L$ mouse results in transcriptional changes in the DG and alterations to cell cycle dynamics, neurogenesis, neuronal maturation, and schizophrenia-related gene expression. Network analyses uncovered latent gene regulatory information and functional logic of gene co-expression networks dysregulated by the mutation. Comparison of the $V_{321}L$ mouse DG transcriptome with human schizophrenia DG transcriptomes using WGCNA revealed ubiquitin ligases as hubs coordinating large protein interaction networks involved in synaptic transmission, RNA processing/trafficking and mitochondrial function.

Genetic variants that influence gene expression, eQTLs, are thought to comprise a substantial proportion of genetic risk in schizophrenia [32]. The cellular mechanisms by which these changes in gene expression influence risk for schizophrenia are not clear. We found a significant enrichment of genes associated with psychotic disorders to be dysregulated in the $V_{321}L$ DG (**Figure 5**). We examined known interaction networks between these genes and found several modular hubs with hub genes represented by the known schizophrenia-associated genes. This larger network of genes was enriched for transcriptional regulators with known regulatory variants associated with schizophrenia. These data are in line with predictions from the omnigenic model wherein core genes/functions are part of densely connected cellular networks of peripheral genes/functions. Additionally, since the core genes involved in synaptic transmission can be accessed by many peripheral genes with cellular homeostatic functions, our data also inform potential mechanisms explaining how peripheral genes might have a cumulative effect on heritability of schizophrenia.

While the diagnosis of schizophrenia is binary, the underlying affected biological processes are quantitative, in a continuous variation. It is then, not surprising that many low effect variants drive heritability of schizophrenia in the population, particularly considering that high effect variants are extremely rare and under strong negative selection [33]. Thus, to derive better insight into the biological mechanisms contributing to schizophrenia and to simultaneously leverage that insight to develop therapeutics, a deeper understanding of molecular signaling networks that link the rare and common variant associated genes is necessary. This approach would help identify key “connectors” or hubs that mediate interactions between synaptic functions (rare variants) and cellular homeostatic functions (common variants), which might be labile to intervention. Intriguingly, while hub genes identified in our SCZ+ network are not obvious mediators of synaptic function (**Figure 5**), half of them have been shown to be part of the hippocampal synaptic proteome in both rodents and humans implicating them as potential mediators linking synaptic function to gene regulatory and cellular homeostatic pathways [34].

Postmortem anatomical analyses and genetic analyses have implicated altered DG function in schizophrenia [31, 35-37]. Additionally, cell type enrichment analyses of schizophrenia-associated gene expression have shown specific enrichment of DG GCs [38, 39]. Adult-born granule cells (abGCs) are important regulators of DG function and have been shown to be necessary for hippocampus-dependent behaviors altered in schizophrenia [40].

Transcriptomic analyses predicted alterations to neurogenesis in the $V_{321}L$ DG, which we confirmed empirically (**Figures 2,3,and 4**). Taken together our results show that in the mutant DG, NSCs exit cell cycle faster and disproportionately commit to a neuronal fate, however, dendritic morphology of immature and mature GCs was altered indicating alterations to development of neuronally committed cells. We noted an upregulation of several gene programs associated with negative regulation of proliferation and positive regulation of neuronal differentiation (**Figure 2-2 and Table 2-2**). Intriguingly the upregulated genes associated with this phenotype were found to be predicted targets of the PRC2, the catalytic subunits (*Eed, Ezh2* and *Suz12*) of which were downregulated in the $V_{321}L$ DG implying a causal relationship. How NRG1 nuclear signaling regulates the expression and/or function of the PRC2 is not known but antagonistic interactions between PRC and the SWI/SNF chromatin remodeling complexes have been noted in the context of

maintaining balance between self-renewal and differentiation of stem cells [41-43]. Interestingly, the NRG1 ICD was shown to interact with BRM, a core ATPase subunit of the SWI/SNF complex and BAF57 another subunit of the SWI/SNF complex in cultured neural stem cells [44]. It is possible that the NRG1 ICD regulates competition between these large remodeling complexes to influence cell fate decisions.

We also noted downregulation of several ribosomal subunit genes and *Cenp* (centromere proteins) genes in the $V_{321}L$ DG (**Figure 2-2 and Table 2-2**). Single cell RNASeq of quiescent and proliferating stem cells in the DG has revealed stereotypical patterns of gene expression as NSCs transitioned from G0 to G1. In particular, it was shown that expression of ribosomal subunit genes and kinetochore genes are upregulated as DG NSCs enter cell cycle [45]. The kinetochore genes and genes related to regulation of microtubule dynamics were predicted to be E2F4 target genes (**Figure 2-2**). E2F family of transcription factors can function as both activators and repressors. E2F4 is one of three canonical E2F repressors along with E2F5 and E2F6 [46]. This implies a potential gain of function of E2F4 in the $V_{321}L$ mutant. Repressor E2Fs have been shown to interact with the PRC and E2F4 accumulates in quiescent cells consistent with its role as a factor that maintains differentiated states [47, 48]. Thus, it is possible that this result is related to mistargeting of PRC and that both, the upregulated and downregulated genes in the $V_{321}L$ mice result from disrupting PRC occupancy across the genome.

Our findings suggest that PRCs might be temporally regulated during neuronal development to target various genes associated with a common function. In line with this, the presence of “polycomb domains”, which are clusters of polycomb proteins bound to DNA segments located several megabases from each other but located in the same 3D space within a nucleus have been demonstrated [49]. These domains are coordinated by CTCF-cohesin complexes [50]. We found that genes dysregulated in the $V_{321}L$ mutant predicted to be regulated by CTCF-cohesin shared functional overlap with the predicted PRC2 target genes (**Figure 2-2**). Our results predict that dysregulation of polycomb occupancy might underlie pathology in schizophrenia. This is supported by the finding that JARID2, which encodes a key regulator of PRC2 targeting, is associated with schizophrenia in multiple populations [51, 52]. Furthermore, expression of EZH1, the methyltransferase in PRC1, is altered in schizophrenia, and is sensitive to antipsychotic medication [53].

Co-regulation of gene expression is a common phenomenon observed throughout evolution [54]. We examined co-expression of genes in the $V_{321}L$ DG using WGCNA and found a large network of genes whose expression co-varied with genotype (**Figure 6-1**). Polycomb-target genes assembled into a module of co-regulated genes with shared functions (**Figure 6-1G**). PPI networks constructed from these WGCNA modules showed an extremely densely connected network (**Figure 6A & 6B**). Strikingly, we observed a very similar profile and high functional overlap when we performed similar analyses on a published dataset of human schizophrenia and healthy control DG granule cell layer transcriptomes [31]. We found that in both $V_{321}L$ mouse and schizophrenia human networks, a core network of ubiquitin-proteosome system (UPS) associated genes formed the hubs (**Figure 6E**).

Most common variants associated with schizophrenia identified in genome-wide association studies (GWAS) have low effect sizes, with the most significant SNPs having odds ratios <1.5 [55]. However recent meta-analyses and large sample studies have been able to identify some ultrarare variants with large effect sizes. One of the highest effect size SNPs is associated with the *CUL1* gene which encodes the ubiquitin ligase CULLIN1 [56, 57]. Several studies have reported altered expression of enzymes involved in protein ubiquitination in postmortem brains from patients with schizophrenia compared to controls [58-60]. Additionally, mutations in other Cullin genes have also been associated with neurodevelopmental disorders like autism [61]. These findings support the hypothesis that regulation of UPS might play a critical role in mediating neurodevelopmental events that underlie the pathology of psychotic disorders.

Our finding that the hubs of upregulated and downregulated networks are members of different multisubunit ubiquitin ligase complexes might argue that loss of NRG1 nuclear signaling produces a shift in types of E3 ubiquitin ligase complexes and thereby alterations to the proteome in specific ways since different complexes have different substrate specificities. Additionally, the striking overlap in the types of E3 ubiquitin complex hubs in both, the $V_{321}L$ mouse DG and DG samples from people with schizophrenia, implicates potential specificity of a “ubiquitinopathy” in schizophrenia. This is further underscored by the finding that the first-degree nodes interacting with the ubiquitin ligase hubs have identical functional enrichments and some overlap in the actual genes as well (**Figure 6F**).

Concluding remarks

ERBB4 binding to NRG1 can act as a signal to generate nuclear ICD clusters and requires functional □-secretase to do so. TYPE III NRG1 and its receptor ERBB4 are synaptic proteins. In the mouse hippocampus, ERBB4 expression is mostly accounted for by different subtypes of interneurons in the DG, which are some of the first synaptic partners of newborn dentate GCs, providing input early during GC maturation [62, 63]. Additionally, GCs strongly innervate GABAergic neurons in the CA3, which are known to express ERBB4 [64, 65]. We propose that ERBB4-regulated nuclear back-signaling might originate at dentate GC axonal pre-synapses. We hypothesize that in neurons, the NRG1 ICD coordinates changes in gene expression as a function of synaptogenic interactions. Mechanistically, this change in gene expression might serve to establish a genomic landscape that signals the dendrites to mature, accept afferents and integrate into a circuit as the axons form synapses on the efferent end.

It has become increasingly evident that psychiatric-disease related risk variants across various disorders aggregate in signaling pathways involved in protein modification such as the UPS and histone modifications [66]. These pathways can be potentially accessed by disease-associated processes directly due to common genetic variants that alter expression of the pathway components, however this alone cannot confer specificity of one disorder over another. We found that that disease-associated pathways can be potentially regulated by a common set of transcriptional regulators such as the PRCs. We propose that these regulators can in turn be regulated by specific developmental signaling mechanisms such as synaptogenic interactions (in this case, in the form of the nuclear ICD). The combination of transcriptional regulators impinging upon gene networks within “risk-associated pathways” and intersecting developmentally regulated signaling events might provide specificity for specific disorders and offer a framework to understand how environmental factors interact with genetic risk associated with disease.

METHODS & MATERIALS

SUPPLEMENTAL MATERIALS AND METHODS

KEY RESOURCES TABLE

REAGENT or RESOURCE	SOURCE	IDENTIFIER
Antibodies		
Rabbit anti-Neuregulin1 B1a (1:500)	Santa Cruz	Cat# sc-348 Lot# D2816, H0403, G122
Mouse anti-Neuregulin1 CRD (1:100)	NeuroMab	Cat# 75-226 Lot# 447 Clone N126B/31
Rabbit anti-Neuregulin1 ß1a (ICC-1:500, WB-1:1000)	This paper	N/A
Rabbit- PROX1 (1:1000)	Abcam	Cat# ab101851
Mouse anti-TuJ (1:1000)	Biolegend/Covance	Cat# MMS-435P
Rabbit anti-Ki67 (1:500)	Abcam	Cat# ab15580 Lot# GR257727-1, GR300154-1
Goat anti-DCX (1:500)	Santa Cruz	Cat# sc-8066 Lot# K1215
Rabbit anti-GFP (1:1000)	LifeTech	Cat# A11122 Lot# 1828014
Rabbit anti-CALB1 (1:500)	Synaptic Systems	Cat# 214003
Rabbit anti-SYNPR (1:500)	Synaptic Systems	Cat# 102003
Rabbit anti-DOCK10 (1:500)	Fisher Scientific (Bethyl Labs)	Cat# 50-156-0039
IRDye800-conjugated Affinity Purified Goat anti-Rabbit IgG (H&L) (1:20,000)	Rockland	Cat# 611-132-002 Lot# 23205
Goat anti-Rabbit Alexa Fluor 680 conjugate (1:30,000)	LifeTech	Cat# A21109 Lot# 433580
Donkey anti-Rabbit Alexa Fluor 488 conjugate (1:1000)	LifeTech	Cat# A21206 Lot# 1910751
Donkey anti-Rabbit Alexa Fluor 594 conjugate (1:1000)	LifeTech	Cat# A21207 Lot# 1668652
Donkey anti-Goat Alexa Fluor 488 conjugate (1:1000)	LifeTech	Cat# A11055 Lot# 412435
Donkey anti-Mouse Alexa Fluor 488 (1:1000)	LifeTech	Cat# A21202 Lot# 41225A, 1796361
Bacterial and Virus Strains		
MMLV (VSV-G)-GFP	Dr.Shaoyu Ge	https://www.nature.com/articles/nature04404
Chemicals, Peptides, and Recombinant Proteins		
BenchStable DMEM	Gibco	Cat# A4192101
Glutamax	Gibco	Cat# 35050061
Recombinant Mouse ErbB4/Her4 Fc Chimera Protein, CF	R&D Systems	Cat# 4387-ER-050
Papain from papaya latex	Sigma	Cat# P4762 Lot# SLBZ8588
BDNF	Gibco	Cat# 10908-010
B-27™ Supplement (50X), serum free	Gibco	Cat# 17504044
Paraformaldehyde, 32% w/v aq. soln., methanol free	Thermo Scientific	Cat# 473779M
DAPI Fluoromount G	Southern Biotech	Cat# 101442-494

Spectral DAPI	Akoya Biosciences	Cat# FP1490
Prolong Gold Antifade	ThermoFisher	Cat# P36934
cOmplete™ Protease Inhibitor Cocktail	Sigma Aldrich	Cat# 11836145001
PhosSTOP™	Sigma Aldrich	Cat# 4906837001
DAPT	CST	Cat# 15020S
RNA*later*™ Stabilization Solution	Invitrogen	Cat# AM7020
Hibernate-A medium	Gibco	Cat# A1247501
Opal 570 Reagent Pack	Akoya Biosciences	Cat# FP1488001KT
Opal 620 Reagent Pack	Akoya Biosciences	Cat# FP1495001KT
Opal 690 Reagent Pack	Akoya Biosciences	Cat# FP1497001KT
Deposited Data		
RNA-Seq data	https://www.ncbi.nlm.nih.gov/geo/query/acc.cgi?acc=GSE192869	GEO Accession code: GSE192869
Raw sequencing reads	This paper	(available on SRA) BioProject ID: PRJNA793574
Experimental Models: Cell Lines		
Neuro-2a (ATCC® CCL-131™)	ATCC	
HEK293-T	ATCC	
Experimental Models: Organisms/Strains		
Mouse: V321L: Nrg1tm1Dat V/L	This paper	
Oligonucleotides		
Genotyping Fwd Primer: 5'-GGTGATCCCATACCCAAGACTCAG-3'	IDT	
Genotyping Rev Primer: 5'-CTGCACATTTATAGAGCATTTATTTTG -3'	IDT	
Type III Nrg1 RNAScope probe: a 19ZZ probe named **Mm-Nrg1-O5** targeting 34-1171 of NM_001364422	ACD/Bio-Techne	This study (custom probe)
Recombinant DNA		
pUX-GFP	Dr.Shaoyu Ge	
pCMV-VSV-G	Dr.Shaoyu Ge	Addgene Plasmid #8454
GP	Dr.Shaoyu Ge	
TypeIII Nrg1-YFP	Dr. Kevin Czaplinski	
Software and Algorithms		
Code for RNASeq analysis	https://github.com/RajNINDS/V321L_DG	

Experimental model and subject details

Male and female mice ages E18.5 - 6 months were used. Animals were housed in a 12-hour light/dark cycle environment that was both temperature and humidity controlled. Animals had free access to food and water. All animal care and experimental procedures were approved by the Institutional Animal Care and Use Committee of the SUNY Research Foundation at Stony Brook University, Stony Brook NY (Protocol #1618) and NINDS, National Institutes of Health, Bethesda MD (Protocol #1490).

Genotyping

Genotypes were determined by PCR using the following primers:
NDEL1 - Forward primer 5'- GGTGATCCCATACCCAAGACTCAG -3'
NDEL2- Reverse primer 5'- CTGCACATTTATAGAGCATTTATTTTG -3'

Antibody generation

Antibodies recognizing the NRG1 intracellular domain were raised in rabbits using the immunizing peptide: DEE(pY)ETTQEYEPAQEP by Biomatik. Antibodies recognizing the phosphorylated peptide DEE(pY)ETTQEYEPAQEP vs. the unphosphorylated peptide DEEYETTQEYEPAQEP were purified by affinity chromatography. Antibody validation can be found in Figure 2-1. A cocktail of antibodies was used for staining cells comprised of antibodies against the phosphorylated and non-phosphorylated peptides.

Nuclear fractionation

For each experiment, cortex, and hippocampus were pooled by genotype for nuclear fractionation. P86-108 animals were deeply anesthetized with isofluorane and decapitated, and cortex and hippocampus were isolated on ice and homogenized with Dounce homogenizer on ice in 5mL nuclear fractionation buffer (60mM KCl, 15mM NaCl, 15mM Tris-HCl pH7.6, 1mM EDTA, 0.2mM EGTA, 15mM 2-mercaptoethanol, 0.5mM spermidine, 0.15 spermine, 0.32M sucrose, cOmplete ULTRA tablets protease inhibitor cocktail). Samples were first homogenized with the loose pestle checking for single, dispersed cells after every 10 strokes using a hemocytometer. Samples were then homogenized with the tight pestle checking for dissociated nuclei after every 10 strokes. Samples were centrifuged at 1000 *xg* for 10 minutes at 4°C. Pellets were resuspended in nuclear fractionation buffer with 0.1% Triton X-100 and incubated on ice for 10 minutes and then pelleted at 1000 *xg* for 10 minutes at 4°C. Pellets were resuspended in 500µL nuclear fractionation buffer, layered over 500µL of a 1M sucrose (in nuclear fractionation buffer) cushion, and centrifuged at 1000 *xg* for 10 minutes at 4°C. Pellets were resuspended in 1mL nuclear fractionation buffer. Laemmli buffer was added to each sample and boiled at 95°C for 5 minutes. Denatured samples were stored overnight at -20°C. Protein analysis was then performed by immunoblot.

Immunoblotting

Samples were electrophoresed on 8% SDS-PAGE gel at 90V for 1.5 hours at room temperature. Proteins were transferred onto nitrocellulose membranes via wet transfer performed at 4°C at 100V for 1 hour. Membranes were blocked in Odyssey Blocking Buffer (LI-COR #927-40000) for 1 hour at room temperature with gentle agitation. Membranes were then incubated overnight on a rocker at 4°C with primary antibodies diluted in 50% blocking buffer. The next day, membranes were washed 3 times with PBS-T (PBS+0.1% Tween20) and incubated with secondary antibodies (diluted in 50% blocking buffer) for 1 hour at room temperature with gentle agitation. After 3 washes in PBS-T, membranes were imaged using the LI-COR Odyssey Infrared Imaging System. Protein signals were then quantified using ImageJ as average grey value in each band.

Cell culture:

Primary neuronal culture: PND4 WT (VV) and $V_{321}L$ (LL) mice were rapidly decapitated, and their brains were transferred to ice-cold Hibernate-A. Hippocampi were dissected out and transferred to Hibernate-A (ThermoFisher Cat# A1247501) on ice. Hibernate solution was removed and replaced with activated and filtered Papain (Sigma Cat# P4762, Lot# SLBZ8588) dissolved in Hibernate-A. Hippocampi were digested for 15min in a 37ºC water bath gently inverting the tube every 5min. Papain solution was removed, and digested tissue was washed thoroughly (4x) with wash solution (Hibernate-A+10%FBS+100U DNase I (StemCellTech. Cat#07469)) by resuspending the tissue in wash solution and allowing it to settle before replacing wash solution. 40µm cell strainers were placed over 50mL conical tubes and wet with plating medium (Neurobasal+B27+Glutamax+Pen/Strep+HEPES) and flowthrough was discarded. Wide and narrow bore fire-polished Pasteur pipettes were pre-wet with FBS and were used to triturate the tissue into a single-cell suspension. The cell-suspension was applied to the pre-wet cell strainer and flow through was collected and analyzed for live/dead cells using Trypan blue on the CountessII automated cell counter. ~100kcells/well were plated into 24 well plates containing 12mm Poly-D-Lysine+Laminin coated coverslips in a total volume of

250µL/well. Neurons were left overnight to adhere, and 250µL fresh plating medium was added the following day to each well. 50% of the total media was replaced every other day until experimental time points.
For cortical cultures, cortices were isolated from 18.5 day old embryos.
Cell line culture and transfection: Neuro2A cells (ATCC) were maintained in DMEM+10%FBS+1:1000 Gentamycin. Cells were passaged on a Mon-Wed-Fri scheduled and were not used beyond 10 passages. Cells were transfected with plasmid DNA using Lipofectamine2000 following manufacturer guidelines. Plasmid details can be found in the Key Resources Table.

Stimulation & drug treatments:

Recombinant Mouse ERBB4/HER4 Fc Chimera Protein was reconstituted at a final concentration of 0.5µM and stored at -80ºC. Working stocks of 0.1µM were prepared and stored briefly at -20ºC. For stimulation experiments, 20nM ERBB4 solution was prepared by diluting 0.1µM stock solution in 125µL Neurobasal plating medium/well.
Neurons were washed by gently swirling the plate and aspirating out all the media and near-simultaneously replacing with 125µL of fresh pre-warmed plating media and equal volume of
Drug concentrations, (pre)treatment periods are listed in the table below:

Drug Name	Manufacturer	Concentration	Treatment Time
DAPT	CST	20µM	24h
ERBB4-ECD	R&D Systems	10nM	15-20min
Wortmannin	Sigma	500nM	45min
L685458	Sigma	5mM	45min

Immunocytochemistry:

Neurons were fixed for 5min at room temperature (RT) in 4% PFA by adding equal volume of 8%PFA to neurobasal in the wells. Entire solution was replaced with fresh 4%PFA and neurons were fixed further for 10min at RT. Coverslips were washed 3x 5min each in 1xPBS-G (PBS+0.1M Glycine), incubating in the final wash for 10min. Neurons were then permeabilized in 0.1% Triton X-100 in 1xPBS for 15min at RT. Coverslips were washed 3x 5min each with 1x PBS-G and incubated in blocking solution (10% normal donkey serum-NDS) for 30min. After blocking, coverslips were incubated with primary antibodies prepared in 1% NDS overnight at 4ºC. Coverslips were washed thoroughly with 1xPBS at RT 3x 5min each and were then incubated with secondary antibodies prepared in 1%NDS+0.1%Triton X-100. Coverslips were washed thoroughly with 1xPBS at RT 3x 5min each and mounted in mounting medium containing DAPI (DAPI Fluoromount-G™ - Southern Biotech). Antibodies used and concentrations can be found in the Key Resources Table (KRT).

Tissue processing and immunohistochemistry:

Animals were deeply anesthetized with isofluorane and transcardially perfused with 4% paraformaldehyde (PFA) in PBS. Brains were harvested and post-fixed overnight at 4°C in 4% PFA in PBS. Brains were transferred to 30% sucrose in PBS and incubated at 4°C with agitation until they sank. Brains were embedded in optimal cutting temperature (O.C.T.) compound, flash frozen and stored at -80°C. 20-50µm sections were obtained serially over the entire dorsoventral extent of the hippocampus, and each slide collected 1 of every 8 (20 µm) or 1 of every 4 sections (50 µm). Sections were dried at room temperature overnight prior to immunohistochemistry.
Antigen retrieval was performed for Ki67 staining by immersing sections in antigen retrieval buffer (10mM sodium citrate, 0.05% Tween20, pH 6.0) at 100°C for 15 minutes. Sections were then allowed to cool to room temperature and neutralized in 0.1M borate buffer, pH8.5 for 10 minutes at room temperature. After 3 5-minute washes in PBS, sections were incubated in blocking buffer (5% normal donkey serum, 0.1% Triton X-100 in PBS) for 1 hour at room temperature. Sections were then incubated with primary antibodies diluted in blocking buffer for 48 hours at 4°C in a humidity chamber. After 3 5-minute washes in PBS, sections were then incubated with secondary antibodies diluted in blocking buffer for 1 hour at room temperature. Sections were

dehydrated in 70% ethanol for 5 minutes and treated with autofluorescence eliminator reagent (Millipore Sigma 2160). No. 1.5 glass coverslips were then mounted on the slides with DAPI Fluoromount-G and allowed to dry overnight at room temperature. For PROX1, CALB1, and SYNPR staining, primary antibody incubation was done for 24h at 4°C and secondary antibody incubation for 2-3 hours at room temperature.
Antibodies used and concentrations can be found in the Key Resources Table (KRT).

Fluorescent in-situ hybridization (FISH):

Brains were fixed and cryosectioned as described earlier. 25µm sections were prepared with one coronal section on a slide containing the dorsal hippocampus. FISH was performed per manufacturer's instructions using the RNAscope v2 fluorescent multiplex assay (ACD/Bio-Techne, CA). Details on the probe used to target the *TypeIII Nrg1* transcript can be found in the KRT.

Imaging & image analysis:

To image NRG1 ICD puncta in the nucleus, imaging was done on the Zeiss LSM800 confocal microscope using the 63x oil immersion objective. All samples were imaged using identical parameters. Neurons to analyze were identified by expression of TYPE III NRG1 (CRD+), and their nuclei were imaged at 2.5x digital zoom with 1µm z-steps.
Image processing and analysis was performed using ImageJ (FIJI). Briefly, center of the nucleus was identified and 1 z-section above and below it was flattened via maximum intensity projection. DAPI-stained nuclei were outlined, and the enclosed area was measured and noted. ICD clusters were manually counted using the cell-counter plugin. Density of clusters was calculated by dividing number of clusters by the nuclear area.
Images examining TYPE III NRG1 expression profile in the dentate gyrus and images used for Ki67+ total cell counts in P21 animals were done using the Optical Fractionator probe on the Stereo Investigator software (MBF Bioscience) coupled to live imaging on an epifluorescent microscope. Section sampling fraction was 1 every 8th section, counting frame size used was 100 µm x 100 µm, and guard zone height used was 10 µm. All sample counts achieved a Gundersen coefficient of error of <0.1.
DCX+ cell density counts were acquired on Olympus FLV1000 confocal microscope at 20X magnification with 3-µm z-steps. Images were analyzed in ImageJ using the Cell Counter plugin. Only cells located in the subgranular zone of the dentate gyrus were counted. Total cell counts for each animal were divided by the total dentate gyrus volume counted to obtain cell density. For each animal, 12-14 coronal sections were sampled along the entire dorsoventral extent of the dentate gyrus.
EdU labeling counts were done on images acquired using Olympus VS-120 microscope at 20X magnification. Images were acquired at 1-µm Z-steps of the entire dentate gyrus hemisection. Images were analyzed in ImageJ using the Cell Counter plugin. Total cell counts for each animal were divided by the total dentate gyrus volume counted to obtain cell density. For each animal, 12-14 coronal sections were sampled along the entire dorsoventral extent of the dentate gyrus.
PROX1, CALB1, DOCK10 and SYNPR stained sections were imaged on a Nikon Ti2 spinning disk confocal microscope using a 40x silicone immersion objective. Images were acquired at 1-µm Z-steps of the dentate gyrus and/or CA3. 3-5 sections per animal were analyzed and averaged. For PROX1, the granule cell layer was outlined as an ROI in ImageJ and the density of average fluorescence intensity (AFI) in the ROI was calculated. For CALB1, the AFI in the field of imaging was calculated, for DOCK10, the molecular layer was outlined as the ROI and integrated density was calculated, and for SYNPR, the mossy fibers staining in CA3 was outlined and the area of the ROI was calculated. Additionally, using DAPI staining, the Slu and Pyr layers of CA3 were identified and delineated as ROIs and AFI/area was calculated.

Golgi impregnation, sampling criteria, imaging, & analysis

P60 animals were deeply anesthetized with isofluorane, and brain samples were harvested quickly on ice and rinsed with ice-cold PBS. The brain samples were then treated with the FD Rapid GolgiStainTM Kit (FD NeuroTechnologies, Inc., catalog # PK401) per manufacturer's guidelines. 100 µm brain sections were collected using a vibratome and dried overnight in the dark at room temperature. Sections were then dehydrated in progressively increasing concentrations of ethanol solution (50% → 75% → 95%), then xylene, and coverslipped with Permount solution.
Imaging of Golgi impregnated neurons in the dentate gyrus was done on the Olympus VS-120 microscope at 60x magnification. Individual neurons were selected for imaging based on the following criteria: 1) the neuron's

cell body resided in the granule cell layer in the intermediate section of the superior blade, 2) the soma morphology assumed the typical granule cell “tear drop” morphology, 3) the dendritic arbor originated from a single primary dendrite and assumed a cone-shaped morphology 4) the dendritic arbor was not obstructed by other cell bodies or dendrites. 11 neurons from 5 wildtype animals and 13 neurons from 5 homozygous mutants were ultimately selected for analysis. Dendritic arbor tracings, sholl analysis, and branching analysis were done on the NeuronStudio software.

GFP-expressing retrovirus production, injection, imaging, & analysis

GFP-retrovirus was prepared by co-transfection of pUX-GFP, VSVG, and GP constructs (kindly provided by the laboratory of Shaoyu Ge; previously described in [63]) into HEK293 cells. Viral supernatant was collected, the retrovirus was concentrated by ultracentrifugation, and the viral pellet resuspended in sterile PBS. Following anesthetization, ~P90 animals were stereotaxically injected bilaterally in dorsal dentate gyrus (-2.0 mm A/P, +1.6 mm M/L, -2.5 mm D/V) and ventral dentate gyrus (-3.0 mm A/P, +2.6 mm M/L, -3.2 mm D/V). The injection volume was 0.25 µL/site. Following surgery, animals were administered 0.03 mL ketorolac (3 mg/mL) for every 10g body weight.

14 days following stereotaxic viral injections, animals were sacrificed, and brain samples harvested as described previously for tissue preparation. 50-µm floating coronal sections were obtained, and each set of sections contained 1 of every 6th section of the hippocampus along its dorsoventral extent.

Analysis was done in real time while imaging on the Zeiss Axio Imager A1 Fluorescent Microscope using a 40x oil immersion objective lens. The identity of GFP+ cells were determined by a combination of morphology, DCX immunoreactivity, and Nissl staining. Neural progenitors were identified by short, tangential processes and the lack of radially oriented processes, with or without DCX immunoreactivity. Immature granule cells were identified by their radially oriented neurites, DCX+ and Nissl+ staining. Astrocytes were identified by their star-like morphology, extensive branch ramifications, and lack of DCX immunoreactivity and Nissl staining.

EdU labeling and tissue processing (cell cycle exit, length, and survival)

To measure cell cycle reentry, EdU (50 µg/g body weight) was injected intraperitoneally in animals at ~P90. 24 hours after EdU injection, animals were sacrificed, and brain samples were harvested and prepared as described in the previous section. To visualize EdU incorporation, the Click-iTTM EdU Cell Proliferation Kit (Thermo Fisher Scientific, catalog # C10338) was used according to manufacturer’s guidelines, followed by immunohistochemistry as described in the previous section.

To measure cell cycle length, EdU (50 µg/g body weight) was injected intraperitoneally in animals at P21-30. 30 minutes after EdU injection, animals were sacrificed, and brain samples were harvested and prepared as described in the cell cycle reentry experiment. To measure newborn cell survival, three pulses of EdU (50 µg/g body weight) spaced 24-hours apart were injected intraperitoneally in animals at ~P90. Animals were sacrificed 30 days later, and brain samples harvested.

RNA sample prep and sequencing

All tools, glassware, gloves, and surfaces were cleaned with ethanol and RNaseZAP™(Invitrogen) according to manufacturer guidelines.

Mice were anesthetized using isoflurane. Mice were then placed in a shallow ice trough and rapidly perfused with 10mL ice-cold 1x phosphate buffered saline (PBS) (total time required from induction of anesthesia to end of perfusion was ~5 min). The brain was immediately removed and transferred to a pre-chilled stainless-steel adult mouse brain matrix placed in ice to make 0.3mm coronal sections (~2min) using pre-chilled blades. The sections were immediately transferred to ice-cold Hibernate-A in a pre-chilled glass petri dish on ice. Dentate gyrus (DG) was visually identified and dissected out from hippocampal sections to isolate the upper and lower blades along with adjoining regions of the hilus and part of the molecular layer (**See Figure 3A**). The microdissections took no more than 3min per brain. Dissected DG bits were transferred to 1mL RNALater in a microcentrifuge tube placed in ice and were left rotating at 4ºC overnight. The following day, tissue was extracted from RNALater solution, flash frozen using dry ice and 100% ethanol and stored at -80ºC until RNA extraction.

RNA was extracted from flash frozen DG bits using the RNeasy Micro Kit (Qiagen) with on-column DNAse treatment following manufacturer guidelines. RNA was poly-A selected and RNA-Seq libraries were prepared using NEBNext Library Prep Kit for Illumina (NEB #E7760). A Miseq shallow sequencing run was performed

after library preparation to balance the sample loading process on the deep sequencer. Sequencing was performed using NSQ 500/550 Hi Output KT v2.5 (150 CYS) (Illumina) to obtain 75bp paired end reads. The estimated read depth was ~33.33 million reads/DG sample.

Differential Gene Expression (DEG) Analysis

QC inspection was performed on sequencing data using a combination of FastQC, MultiQC, and Fastx_Screen. Next, adaptor sequences were clipped and low quality and/or nucleotide biased positions in sequences were trimmed using the Trimmomatic; QC inspection of the post clipped and trimmed sequences was repeated. Clipped and trimmed sequences were aligned to the mouse reference genome (mm10) using the HISAT2 tool and QC inspection of the alignments was performed using the RSeqC. Transcript assembly was performed using StringTie which included the discovery of any novel genes:isoforms. QC inspection of the assembly was performed using the gffcompare tool. To enumerate both gene-level and transcript-level expression from the assembly output, IsoformSwitchAnalyzeR package supported in R was used. For differential analysis of the enumerated gene-level expression, commands and functions supported in R were used. Briefly, expression per sample was first within sample normalized via cpm (counts per million) then pedestalled by 2 by taking the log2 transformation. To correct for differences in spread and location, required before testing, cross-sample normalization was performed using Cyclic Lowess. Expression after normalization was inspected by cov-based PCA scatterplot to identify any outliers. Using this 1 sample was identified as an outlier (WT female). This sample was further inspected for coverage using a set of house-keeping genes in mm10 and was found to be 5' degraded and as such was excluded from further analysis. Other samples were reinspected for coverage and were found to pass QC. Normalization for the gene-level expression was repeated after outlier removal, and sequence batch was globally corrected for via the Limma tool. Using the noise model plot generated from Limma, we identified a mean batch-corrected normalized expression value of 2.25 that was then used to filter genes and transcripts not having at least one sample greater than this value while also flooring values to 2.25 for surviving genes and transcripts if less than this value. These filter-floored values for surviving transcripts were tested for differential expression between WT and $V_{321}L$ samples via ANCOVA controlling for sequence batch and biological sex. Dysregulated genes were identified as those having a p-value of <0.05 or <0.1 (colored differently on volcano plot) corrected for batch and/or sex and a minimum fold-change of 1.25 in either direction. Dysregulated genes were then used to perform enrichment analyses using Ingenuity Pathway Analysis (IPA) (Qiagen) and Enrichr [20, 21, 23]. WGCNA was conducted using the R package (detailed code can be found on the Github link provided below).

Network analyses

Schizophrenia-related enriched terms were combined into a single pathway in IPA yielding 67 genes. These 67 genes were selected as seeds and a network was grown using the Build>Grow tool in IPA. The following criteria were set to grow the network: Direct interactions only using the DEG list from the $V_{321}L$ vs. WT dataset, using all data sources within the IPA knowledge base, for miRNAs we selected only those that were experimentally observed. For data from cell lines and tissues, we selected only data from CNS cell lines, neuroblastoma cell lines, and neurons using the stringent filter setting to ensure that two nodes will only be connected if the genes are expressed in neural cells. We also excluded "correlation" and "membership" as relationship criteria for connecting nodes leaving behind direct physical or signaling interactions.

Genes from WGCNA modules were used to generate PPI networks using STRING [28]. We adjusted the settings to only include interactions from experiments, databases, and gene fusions. Minimum required interaction score was set to 0.9 (highest stringency) and disconnected nodes were removed.

Networks were exported to Cytoscape and hub gene analysis was performed using the CytoHubba plugin.

Statistical analysis

Statistical analysis was performed using Prism (GraphPad). Normality was assessed using Shapiro-Wilkins and Kolmogorov-Smirnov tests. If data failed either test, non-parametric stats were used. p-values were corrected for multiple comparisons as necessary using Bonferroni (parametric) post-hoc test.

For Sholl analysis we followed published guidelines to avoid faulty inferences in Sholl analyses [67]. Sholl analysis data did not pass Shapiro-Wilkins normality test; however, given that measurements were made from multiple neurons from the same animal pooled with neurons across animals, we could not use the Wilcoxon rank sum test given the assumption of independence of variables. To address this, we transformed the data by taking the square-root of the measurements and used a repeated measures two-way ANOVA with a mixed effects model. To control for false discovery rate (FDR) and Type I error inflation, p-values were corrected for multiple comparisons using the original Benjamini-Hochberg FDR procedure.

RESOURCE AVAILABILITY

Lead Contact

Further information and requests for resources and reagents should be directed to and will be fulfilled by Lead Contact, Dr. David Talmage (david.talmage@nih.gov).

Materials Availability

Plasmids used in this study have been deposited to Addgene and will be available upon publication under Talmage Lab.

Data and Code Availability

The data generated in this publication have been deposited in NCBI's Gene Expression Omnibus [68] and are accessible through GEO Series accession number GSE192869 (https://www.ncbi.nlm.nih.gov/geo/query/acc.cgi?acc=GSE192869).

Code is available at https://github.com/RajNINDS/V321L_DG

REFERENCES

1. Mei, L. and W.C. Xiong, *Neuregulin 1 in neural development, synaptic plasticity and schizophrenia.* Nat Rev Neurosci, 2008. **9**(6): p. 437-52.
2. Bao, J., et al., *Back signaling by the Nrg-1 intracellular domain.* Journal of Cell Biology, 2003. **161**(6): p. 1133–1141.
3. Hancock, M.L., et al., *Presynaptic type III neuregulin1-ErbB signaling targets alpha7 nicotinic acetylcholine receptors to axons.* J Cell Biol, 2008. **181**(3): p. 511-21.
4. Harrison, P.J. and D.R. Weinberger, *Schizophrenia genes, gene expression, and neuropathology: On the matter of their convergence*, in *Molecular Psychiatry*. 2005. p. 40-68.
5. Walsh, T., et al., *Rare structural variants disrupt multiple genes in neurodevelopmental pathways in schizophrenia.* Science, 2008. **320**(5875): p. 539-43.
6. Agarwal, A., et al., *Dysregulated expression of neuregulin-1 by cortical pyramidal neurons disrupts synaptic plasticity.* Cell Reports, 2014. **8**(4).
7. Talmage, D.A., *Mechanisms of Neuregulin Action*, in *Growth Factors and Psychiatric Disorders*. 2008. p. 74.
8. Chen, Y., et al., *Intramembranous valine linked to schizophrenia is required for neuregulin 1 regulation of the morphological development of cortical neurons.* Journal of Neuroscience, 2010. **30**(27): p. 9199 –9208.
9. Fazzari, P., et al., *Cell autonomous regulation of hippocampal circuitry via Aph1b-γ-secretase/neuregulin 1 signalling.* eLife, 2014. **3**.
10. Wolpowitz, D., et al., *Cysteine-rich domain isoforms of the neuregulin-1 gene are required for maintenance of peripheral synapses.* Neuron, 2000. **25**(1): p. 79-91.

11. Nason, M.W., Jr., et al., *Disrupted activity in the hippocampal-accumbens circuit of type III neuregulin 1 mutant mice.* Neuropsychopharmacology, 2011. **36**(2): p. 488-96.
12. Walss-Bass, C., et al., *A Novel Missense Mutation in the Transmembrane Domain of Neuregulin 1 is Associated with Schizophrenia.* Biological Psychiatry, 2006. **60**(6): p. 548-53.
13. Fleck, D., et al., *Proteolytic processing of neuregulin 1 type III by three intramembrane-cleaving proteases.* Journal of Biological Chemistry, 2016. **291**(1): p. 318-33.
14. Hu, N., et al., *Hippocampal subfield alterations in schizophrenia: A selective review of structural MRI studies*, in *Biomarkers in Neuropsychiatry*. 2020. p. 10.
15. Provenzano, F.A., et al., *Hippocampal Pathology in Clinical High-Risk Patients and the Onset of Schizophrenia.* Biological Psychiatry, 2020. **87**(3): p. 234-242.
16. Iwano, T., et al., *Prox1 postmitotically defines dentate gyrus cells by specifying granule cell identity over CA3 pyramidal cell fate in the hippocampus.* Development, 2012. **139**(16): p. 3051-62.
17. Jaudon, F., et al., *The RhoGEF DOCK10 is essential for dendritic spine morphogenesis.* Mol Biol Cell, 2015. **26**(11): p. 2112-27.
18. Singec, I., et al., *Synaptic vesicle protein synaptoporin is differently expressed by subpopulations of mouse hippocampal neurons.* J Comp Neurol, 2002. **452**(2): p. 139-53.
19. Amaral, D.G. and M.P. Witter, *The three-dimensional organization of the hippocampal formation: a review of anatomical data.* Neuroscience, 1989. **31**(3): p. 571-91.
20. Chen, E.Y., et al., *Enrichr: Interactive and collaborative HTML5 gene list enrichment analysis tool.* BMC Bioinformatics, 2013. **14**: p. 1471-2105.
21. Kuleshov, M.V., et al., *Enrichr: a comprehensive gene set enrichment analysis web server 2016 update.* Nucleic Acids Research, 2016. **44**(1).
22. Lachmann, A., et al., *ChEA: Transcription factor regulation inferred from integrating genome-wide ChIP-X experiments.* Bioinformatics, 2010. **26**(19): p. 2438-44.
23. Xie, Z., et al., *Gene Set Knowledge Discovery with Enrichr.* Current Protocols, 2021. **1**(3): p. e90.
24. Altman, J. and G.D. Das, *Autoradiographic and histological evidence of postnatal hippocampal neurogenesis in rats.* Journal of Comparative Neurology, 1965. **124**(3): p. 319-336.
25. Ming, G.L. and H. Song, *Adult neurogenesis in the mammalian central nervous system*, in *Annual Review of Neuroscience*. 2005. p. 223-50.
26. Chen, Y., L.W. Role, and D.A. Talmage, *Mutant Models of Nrg1 and ErbB4: Abnormalities of Brain Structures, Functions, and Behaviors Relevant to Schizophrenia*, in *The Origins of Schizophrenia*. 2016. p. 382.
27. Kos, M.Z., et al., *Dopamine perturbation of gene co-expression networks reveals differential response in schizophrenia for translational machinery.* Translational Psychiatry, 2018. **8**(1): p. 14.
28. Szklarczyk, D., et al., *The STRING database in 2023: protein-protein association networks and functional enrichment analyses for any sequenced genome of interest.* Nucleic Acids Research, 2023. **51**(1 D): p. D638–D646.
29. Chin, C.H., et al., *cytoHubba: Identifying hub objects and sub-networks from complex interactome.* BMC Systems Biology, 2014. **8**(4).
30. Ripke, S., et al., *Biological insights from 108 schizophrenia-associated genetic loci.* Nature, 2014. **511**(7510): p. 421-427.
31. Jaffe, A.E., et al., *Profiling gene expression in the human dentate gyrus granule cell layer reveals insights into schizophrenia and its genetic risk.* Nature Neuroscience, 2020: p. 510-519.
32. Richards, A.L., et al., *Schizophrenia susceptibility alleles are enriched for alleles that affect gene expression in adult human brain.* Molecular Psychiatry, 2012. **17**(2): p. 193-201.
33. Liu, C., et al., *Interrogating the Evolutionary Paradox of Schizophrenia: A Novel Framework and Evidence Supporting Recent Negative Selection of Schizophrenia Risk Alleles.* Front Genet, 2019. **10**: p. 389.
34. Koopmans, F., et al., *Comparative Hippocampal Synaptic Proteomes of Rodents and Primates: Differences in Neuroplasticity-Related Proteins.* Frontiers in Molecular Neuroscience, 2018. **11**.
35. Tamminga, C.A., A.D. Stan, and A.D. Wagner, *The hippocampal formation in schizophrenia*, in *American Journal of Psychiatry*. 2010. p. 1178-93.

36. Tavitian, A., W. Song, and H.M. Schipper, *Dentate Gyrus Immaturity in Schizophrenia.* Neuroscientist, 2019. **25**(6): p. 528-547.
37. Wang, K., et al., *In vivo analyses reveal hippocampal subfield volume reductions in adolescents with schizophrenia, but not with major depressive disorder.* Journal of Psychiatric Research, 2023. **165**: p. 56-63.
38. Bryois, J., et al., *Genetic identification of cell types underlying brain complex traits yields insights into the etiology of Parkinson's disease.* Nature Genetics, 2020. **52**(5): p. 482-493.
39. Skene, N.G., et al., *Genetic identification of brain cell types underlying schizophrenia.* Nature Genetics, 2018. **50**(6): p. 825-833.
40. Gonçalves, J.T., S.T. Schafer, and F.H. Gage, *Adult Neurogenesis in the Hippocampus: From Stem Cells to Behavior*, in *Cell*. 2016. p. 897-914.
41. Kadoch, C., R.A. Copeland, and H. Keilhack, *PRC2 and SWI/SNF Chromatin Remodeling Complexes in Health and Disease*, in *Biochemistry*. 2016. p. 1600-14.
42. Seo, S. and K.L. Kroll, *Geminin's double life: Chromatin connections that regulate transcription at the transition from proliferation to differentiation*, in *Cell Cycle*. 2006. p. 374-9.
43. Weber, C.M., et al., *mSWI/SNF promotes Polycomb repression both directly and through genome-wide redistribution.* Nature Structural and Molecular Biology, 2021. **28**(6): p. 501-511.
44. Pirotte, D., et al., *Neuregulin-1 modulates the differentiation of neural stem cells in vitro trough an interaction with the Swi/Snf complex.* Molecular and Cellular Neuroscience, 2010. **43**(1): p. 72-80.
45. Shin, J., et al., *Single-Cell RNA-Seq with Waterfall Reveals Molecular Cascades underlying Adult Neurogenesis.* Cell Stem Cell, 2015. **17**(3): p. 360-72.
46. Chen, H.Z., S.Y. Tsai, and G. Leone, *Emerging roles of E2Fs in cancer: An exit from cell cycle control*, in *Nature Reviews Cancer*. 2009. p. 785-797.
47. Cuitiño, M.C., et al., *Two Distinct E2F Transcriptional Modules Drive Cell Cycles and Differentiation.* Cell Reports, 2019. **27**(12): p. 3547-3560.
48. Trimarchi, J.M., et al., *The E2F6 transcription factor is a component of the mammalian Bmi1-containing polycomb complex.* Proceedings of the National Academy of Sciences of the United States of America, 2001. **98**(4): p. 1519-24.
49. Blackledge, N.P. and R.J. Klose, *The molecular principles of gene regulation by Polycomb repressive complexes*, in *Nature Reviews Molecular Cell Biology*. 2021. p. 815-833.
50. Rhodes, J.D.P., et al., *Cohesin Disrupts Polycomb-Dependent Chromosome Interactions in Embryonic Stem Cells.* Cell Reports, 2020. **30**(3): p. 820-835.
51. Chen, G., et al., *Whole genome association study in a homogenous population in Shandong peninsula of China reveals JARID2 as a susceptibility gene for schizophrenia.* Journal of Biomedicine and Biotechnology, 2009. **2009**: p. 1-7.
52. Pedrosa, E., et al., *Positive association of schizophrenia to JARID2 gene.* American Journal of Medical Genetics, Part B: Neuropsychiatric Genetics, 2007. **144**(1): p. 45-51.
53. Johnstone, A.L., et al., *EZH1 is an antipsychotic-sensitive epigenetic modulator of social and motivational behavior that is dysregulated in schizophrenia.* Neurobiology of Disease, 2018. **119**: p. 149-158.
54. Montavon, T., et al., *A regulatory archipelago controls hox genes transcription in digits.* Cell, 2011. **147**(5): p. 1132-45.
55. Nakazawa, T., *Modeling schizophrenia with iPS cell technology and disease mouse models*, in *Neuroscience Research*. 2022. p. 46-52.
56. Legge, S.E., et al., *Genetic architecture of schizophrenia: A review of major advancements*, in *Psychological Medicine*. 2021. p. 2168-2177.
57. Singh, T., et al., *Rare coding variants in ten genes confer substantial risk for schizophrenia.* Nature, 2022. **604**(7906): p. 509-518.
58. Bousman, C.A., et al., *Preliminary evidence of ubiquitin proteasome system dysregulation in schizophrenia and bipolar disorder: Convergent pathway analysis findings from two independent samples.* American Journal of Medical Genetics, Part B: Neuropsychiatric Genetics, 2010. **153**(2): p. 494-502.
59. Luza, S., et al., *The ubiquitin proteasome system and schizophrenia*, in *The Lancet Psychiatry*. 2020. p. 528-537.

60. Rubio, M.D., et al., *Dysfunction of the ubiquitin proteasome and ubiquitin-like systems in schizophrenia.* Neuropsychopharmacology, 2013. **38**(10): p. 1910–1920.
61. Amar, M., et al., *Autism-linked Cullin3 germline haploinsufficiency impacts cytoskeletal dynamics and cortical neurogenesis through RhoA signaling.* Molecular Psychiatry, 2021. **26**(7): p. 3586–3613.
62. Neddens, J. and A. Buonanno, *Selective populations of hippocampal interneurons express ErbB4 and their number and distribution is altered in ErbB4 knockout mice.* Hippocampus, 2010. **20**(6): p. 724-44.
63. Ge, S., et al., *GABA regulates synaptic integration of newly generated neurons in the adult brain.* Nature, 2006. **439**(7076): p. 589-593.
64. Acsády, L., et al., *GABAergic cells are the major postsynaptic targets of mossy fibers in the rat hippocampus.* Journal of Neuroscience, 1998. **18**(9): p. 3386–3403.
65. Vullhorst, D., et al., *Selective expression of ErbB4 in interneurons, but not pyramidal cells, of the rodent hippocampus.* Journal of Neuroscience, 2009. **29**(39): p. 12255-64.
66. O'dushlaine, C., et al., *Psychiatric genome-wide association study analyses implicate neuronal, immune and histone pathways.* Nature Neuroscience, 2015. **18**(2): p. 199-205.
67. Wilson, M.D., et al., *Valid statistical approaches for analyzing sholl data: Mixed effects versus simple linear models.* Journal of Neuroscience Methods, 2017. **279**: p. 33-43.
68. Edgar, R., M. Domrachev, and A.E. Lash, *Gene Expression Omnibus: NCBI gene expression and hybridization array data repository.* Nucleic Acids Research, 2002. **30**(1): p. 207-10.

FIGURE LEGENDS

Figure 1: Generation of NRG1 $V_{321}L$ knock-in mice.

(A) A schematic diagram of the *Nrg1* genomic structure. The *Nrg1* gene encodes six families of isoforms as a result of alternative promoter usage. Types I, II, IV and V contain an Ig-like domains (encoded by exons 3 & 4). Exon 7 is the unique 5-prime coding exon for Type III Nrg1, encoding an N-terminal, cysteine-rich transmembrane domain. Exon 8, in combination with exon 9 or 10, and various combinations of exons 11, 12, and 13, encodes an EGF-like domain common to all Nrg1 isoforms. Exon 13 encodes a common C-terminal transmembrane domain. The C-terminal intracellular domain is encoded by exons 14-17. The missense SNP that results in a valine-to-leucine substitution in the C-terminal transmembrane domain Is shown above the gene.

(B) Schematic diagram of the BAC clone used for generating the target construct corresponding to a region of the Nrg1 gene that comprises the entire Type III coding region. Below the BAC clone is a diagram of the targeting construct, including a 5.8-kbp left homology arm, a neoR cassette in the antisense orientation flanked by Frt sites, and a 2.5-kbp right homology arm.

(C) Diagram showing wildtype and mutant alleles (the mutant following flippase removal of the neo cassette). The C-terminal transmembrane domain sequence is underlined. Black arrows labeled "NDEL1" and "NDEL2" indicate approximate genomic locations of genotyping primers.

(D) An example genotyping gel of offspring from a het x het cross illustrating a wildtype, heterozygote and homozygote.

(E) The mutant mouse line was maintained by breeding heterozygotes. The genotype of pups from >100 litters was analyzed for deviation from the expected 1:2:1 ratio. No deviation was found. Mice with the genotype V/V are referred to as WT in the manuscript and L/L are referred to as $V_{321}L$ as denoted in parenthesis.

Figure 2: Transcriptomic analysis of $V_{321}L$ DG.

(A) Schematic and representative image of DG dissection from hippocampal slices; Mo= molecular layer, GCL= granule cell layer, Hi= hilus.

(B) Volcano plot for differentially expressed genes between $V_{321}L$ and WT DG. Each datapoint represents a single gene. Colored points delineate fold change of at least 1.25 (blue dots – downregulated, red dots- upregulated in the mutant samples) with an adjusted p-value <0.1, and dark colored points represent those with ANCOVA adjusted p-value <0.05. (N=6 mice/genotype. 3 Male/3 Female). *Prox1* and *Calb1* were chosen for validation via immunohistochemistry (IHC).

(C) Left, Immunohistochemical validation of downregulated DG marker genes *Prox1* and *Calb1* in WT and $V_{321}L$; Right, Quantification of PROX1 and CALB1 immunoreactivity (signal density) in the granule cell layer of WT and $V_{321}L$ mice shows significant reduction in PROX1 (p=0.029, Mann-Whitney U=0), scale bar=10µm; and CALB1 (p=0.029, Mann-Whitney U=0), protein expression in the $V_{321}L$ DG (N=4 mice/genotype). (Scale bar=50µm and scale bar=10µm for inset).

(D) Statistically enriched (adj. p (q)<0.05) functional terms from Ingenuity Pathway Analysis (IPA) for differentially expressed genes between $V_{321}L$ and WT DGs. Enriched terms representing dendritic morphology and proliferation of neuronal cells- features chosen for further investigation in this manuscript were selected to be displayed. A few differentially expressed genes grouped under the respective terms are provided as examples within the plot.

(E) Statistically significantly enriched disease terms from IPA for the differentially expressed gene list. Significant terms associated with schizophrenia were selected for display with a few genes grouped under those terms. Complete list of enriched terms and statistics are available in supplementary tables S2 and S3. Complete list of dysregulated genes can be found in supplementary table S1.

Figure 3: $V_{321}L$ DG shows reduced stem cell proliferation, increased cell cycle exit and commitment to neuronal fate.

(A) Left, immunohistochemistry of Ki67 (green), a marker for proliferation, in the DG of P22 WT and $V_{321}L$ littermates and cage mates, merged with DAPI (blue) counterstain, scale bar=100µm. Inset shows a higher magnification image with arrowheads indicating Ki67+ proliferating cells in the subgranular zone of the DG, scale bar=50µm. **Right,** stereological quantification of Ki67+ populations in the DG of P21 WT and $V_{321}L$ (WT N= 6 mice, $V_{321}L$ N= 5 mice; p=0.0271, Welch's t-test. t=2.697, df=8.050).

(B) Left, doublecortin (DCX) immunoreactivity (green) merged with DAPI (blue) counterstain in DG of WT and $V_{321}L$ mice. Inset shows higher magnification image of the region delineated in the white box; arrowheads point to DCX+ cells in the DG. **Right,** quantification of DCX+ population from confocal images of subsampled, coronal DG sections. Confocal images were acquired in 3-µm z-steps from 20-µm coronal sections, and 4-10 images were quantified for each animal (P60-P180 WT N= 11 mice, $V_{321}L$ =10 mice, p= 0.9865, Welch's t-test. t=0.017, df=18.68).

(C) Left, Image from a WT DG showing neural progenitors in S phase of the cell cycle labeled with EdU by intraperitoneal injection (50µg EdU/g body weight) in ~P90 animals. 24 hours post-injection, samples were harvested and processed to detect Ki67 immunoreactivity. EdU and Ki67 co-immunoreactivity indicates that cells remained in the cell cycle 24 hours post-injection (yellow arrowheads). EdU immunoreactivity without Ki67 expression indicates that cells exited the cell cycle (red arrowheads). Ki67 immunoreactivity alone indicates cells that were not in S phase at the time of injection but were in the cell cycle at the time of tissue harvest. **Right,** Quantification of cell cycle reentry by computing the proportion of cells that remained in the cell cycle (EdU+ Ki67+) out of all cells in S phase of the cell cycle at the time of labeling (EdU+ cells). Epifluorescent images were acquired in 1-µm z-steps from 20-µm coronal sections, and 12-14 sections were quantified for each animal (WT N= 6 mice. $V_{321}L$ N=5 mice, p= 0.0043, Mann-Whitney Rank Sum Test U=0).

(D) Left, Image from a WT DG showing neural stem cells infected with a replication-deficient GFP-expressing retrovirus via stereotaxic injection, followed by 14 days of incubation to label NPs and their progeny. The identity of GFP+ cells were determined by a combination of morphology, DCX immunoreactivity, and Nissl

staining. Neural progenitors (NPs) were identified by the lack of radially oriented processes with or without DCX immunoreactivity (open arrowheads). Immature granule cells (iGCs) were identified by their radially oriented neurites, DCX+ and Nissl+ staining (filled, yellow arrowheads). Astrocytes were identified by their star-like morphology and lack of DCX immunoreactivity and Nissl staining (yellow arrows). **Right,** Fate specification was quantified as proportion of GFP+ cells that remained radial glial-like stem cells, NPs, or committed to neuronal or astroglial fates. 5-14 50-µm sections were quantified from each animal, depending on infection efficiency (WT N=3 mice, $V_{321}L$ N=4 mice; Two-way ANOVA Genotype x Cell Fate p=0.0003 F(3, 20)=9.864. NP, WT vs. $V_{321}L$ Bonferroni-corrected p=0.0026. iGC, WT vs. $V_{321}L$ Bonferroni-corrected p=0.0069. RGL & Astrocyte comparisons between genotypes were not significant p>0.9999).

Figure 4: Granule cells produced in the $V_{321}L$ DG display aberrant dendritic arborization.

(A) Left, Doublecortin (DCX - green) immunohistochemistry in the P72 DG along with DAPI counterstain (blue), with high magnification of the dotted white boxes in the middle. **Right,** Representative tracings of DCX+ cells in WT and $V_{321}L$ DG.

(B) Representative tracings of Golgi-impregnated DG granule cells (GCs) from ~P60 WT and $V_{321}L$. Neurites are color coded by branch order (1°= red, 2°= orange, 3°= yellow, 4°= green, 5°= blue, 6°= purple, 7°= pink). Two representative neurons are shown for each genotype (left) one representative of the population average and (right) one representative of neurons with the highest degree of branching. Arrows following the color code outlined above highlight the absence of higher order branching in $V_{321}L$ GCs.

(C) Length of dendritic segments within each zone were summed. Sholl analysis reveals difference in distribution of dendritic lengths in $V_{321}L$ mice. Shaded region around the line represents standard deviation. Data is compiled from 11 neurons from 5 WT animals and 13 neurons from 5 $V_{321}L$ at ~P60. (Mixed effects model Two-way RM ANOVA Genotype x Distance from soma #p=0.0347, F(16, 352)=1.763 ; WT vs. $V_{321}L$ at 80µm away from soma FDR corrected *q=0.0511).

(D.) Proportion of neurons in which 5th, 6th, and 7th order branching are present. $V_{321}L$ granule cells had fewer branches at the higher orders of branching (5th order, p=0.0131; 6th order, p= 0.0817; 7th order, p=0.458; Fisher's exact test). (Wildtype N=11 neurons/ 5 mice, $V_{321}L$ N=13 neurons/ 5 mice).

Figure 5: Dysregulation of a schizophrenia-susceptibility gene network in the $V_{321}L$ DG.

(A) Workflow outlining the generation and analysis of a schizophrenia-susceptibility gene network.

(B) Orthologs of genes associated with schizophrenia spectrum disorders (Figure 2E- IPA analysis) were found to be dysregulated in the $V_{321}L$ DG. A network was grown by seeding schizophrenia-related dysregulated genes ($V_{321}L$ vs. WT) along with the remaining set of differentially expressed genes between $V_{321}L$ and WT DG, in IPA. We labeled this network – SCZ+. Node colors represent fold change in expression (-7.1 blue to 7.1 red) according to heatmap. This network was subjected to hub gene analysis using the mean clique clustering (MCC) method. See Table S5 for a list of genes that are part of the SCZ+ network.

(C) Network display of 10 hub genes identified by MCC analysis of the SCZ+ network, along with their first-degree neighbors (lavender nodes) shows a hub-spoke connectivity with schizophrenia-related genes forming hubs. Hub node color reflects MCC rank.

(D) Top, Hub genes identified in Figure5C were deleted from the SCZ+ network, disconnected nodes were removed from the network and the resulting network is displayed. **Bottom,** Quantification of number of connected components and edges in the SCZ+ network and Hub-deleted SCZ+ network. Node colors represent fold change in expression (-7.1 blue to 7.1 red) according to heatmap.

Figure 6: Shared functional risk profile between $V_{321}L$ mutant mouse DG and DG of people with schizophrenia.

Protein-protein interaction (PPI) networks were constructed (See methods for details) from WGCNA modules. Resulting networks were densely interconnected. Nodes are color coded according to expression levels indicated by the heatmaps in the respective graphs. Edges were bundled for clarity.

(A) mouseUP PPI Network: PPI network from genes positively correlated (upregulated) with the $V_{321}L$ genotype (1910 nodes, average node degree=3.2, PPI enrichment p value= 3.56e-13). Node color legend: fold-change 1 white to 9 deep red.

(B) mouseDOWN PPI Network: PPI network from genes negatively correlated (downregulated) with the $V_{321}L$ genotype (1870 nodes, average node degree=4.7, PPI enrichment p value < 1.0e-16). Node color legend: fold-change -8 blue to 1 white.

(C) humanUP PPI Network: PPI network from genes positively correlated (upregulated) with schizophrenia diagnosis (1364 nodes, average node degree= 8.96, PPI enrichment p value= 1.96e-07). Node color legend: fold-change 1 white to 1.14 deep red.

(D) humanDOWN PPI Network: PPI network from genes negatively correlated (downregulated) with schizophrenia diagnosis (1947 nodes, average node degree= 23.56, PPI enrichment p value= <1.0e-16). Node color legend: fold change -1.2 blue to 1 white.

(E) PPI networks in (A-D) were analyzed using MCC to find top 10 hub genes. All networks except for the human downregulated network had nodes that co-ranked for rank 1 (red). The human down network had 1 rank 1 hub gene (*RPS27A*- red) and the other 9 were co-ranked for rank 10 (yellow). All hub genes were interconnected and were identified as ubiquitin ligases or accessory factors.

(F) Gene Ontology analysis of the up and downregulated genes that comprised the hub genes identified in panel E and their first-degree neighbors from human and mouse networks showed complete overlap of biological processes predicted to be altered. Examples of common differentially expressed genes between species are displayed.

Figure 1

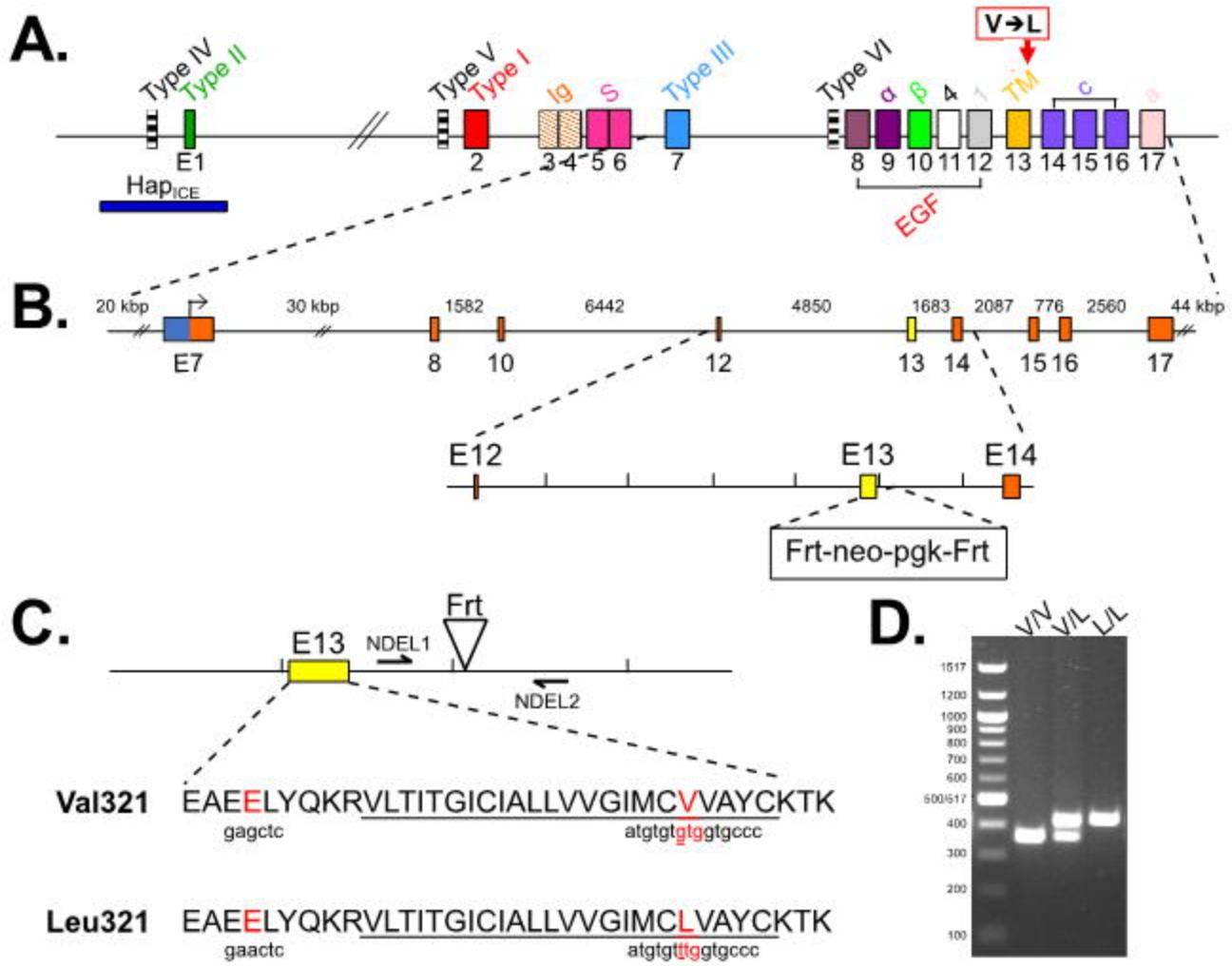

E.

Genotype	Observed	Expected	
V/V (WT)	202	213.5	
V/L	439	427	
L/L ($V_{321}L$)	213	213.5	
		X^2 = 0.958	p= 0.6195

Figure 2

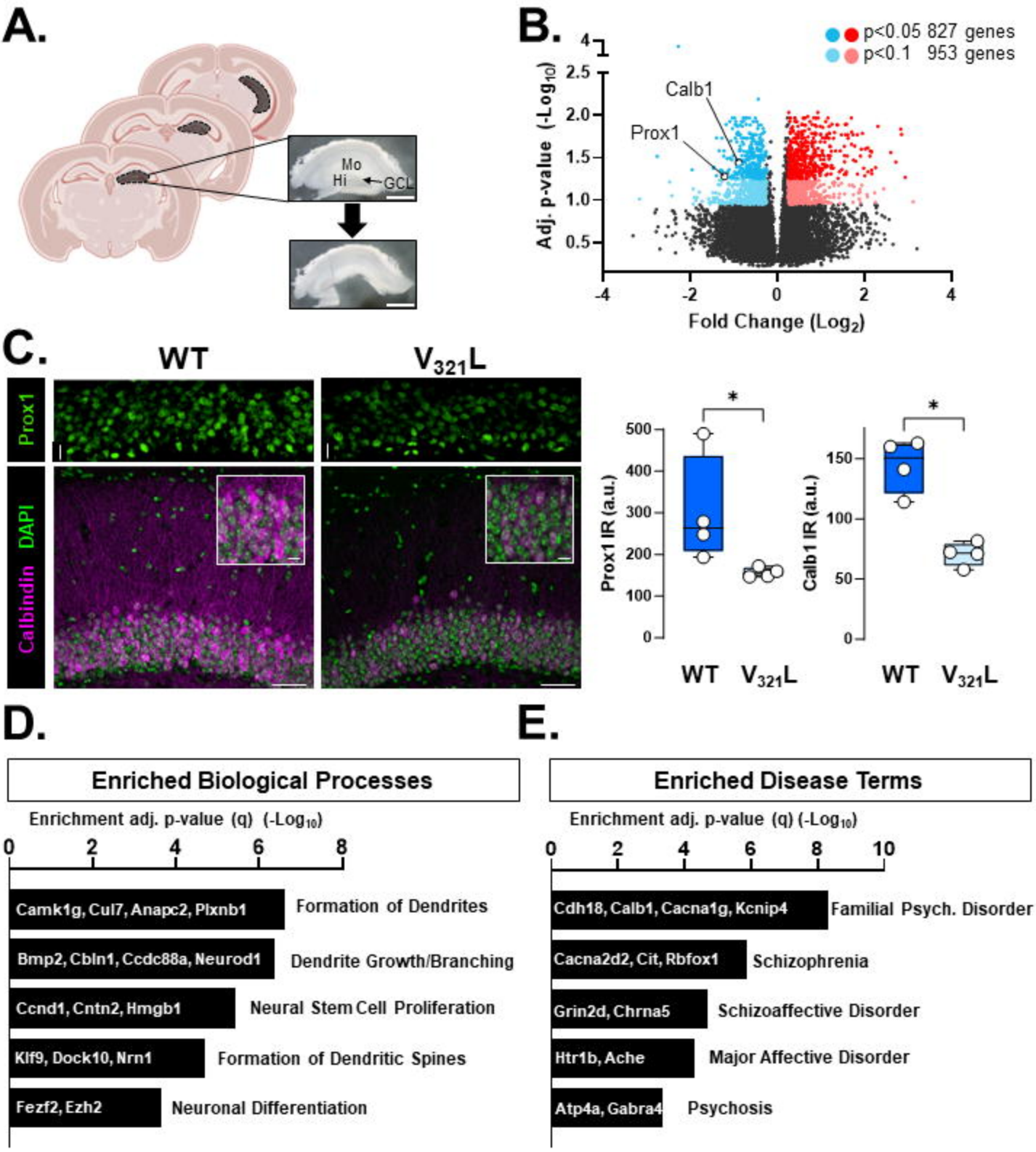
A.
Mo
Hi
GCL
B.
p<0.05 827 genes
p<0.1 953 genes
Calb1
Prox1
Adj. p-value (-Log10)
Fold Change (Log2)
C.
WT
V321L
Prox1
Calbindin DAPI
Prox1 IR (a.u.)
Calb1 IR (a.u.)
WT
V321L
D.
Enriched Biological Processes
Enrichment adj. p-value (q) (-Log10)
Camk1g, Cul7, Anapc2, Plxnb1
Formation of Dendrites
Bmp2, Cbln1, Ccdc88a, Neurod1
Dendrite Growth/Branching
Ccnd1, Cntn2, Hmgb1
Neural Stem Cell Proliferation
Klf9, Dock10, Nrn1
Formation of Dendritic Spines
Fezf2, Ezh2
Neuronal Differentiation
E.
Enriched Disease Terms
Enrichment adj. p-value (q) (-Log10)
Cdh18, Calb1, Cacna1g, Kcnip4
Familial Psych. Disorder
Cacna2d2, Cit, Rbfox1
Schizophrenia
Grin2d, Chrna5
Schizoaffective Disorder
Htr1b, Ache
Major Affective Disorder
Atp4a, Gabra4
Psychosis

Figure 3

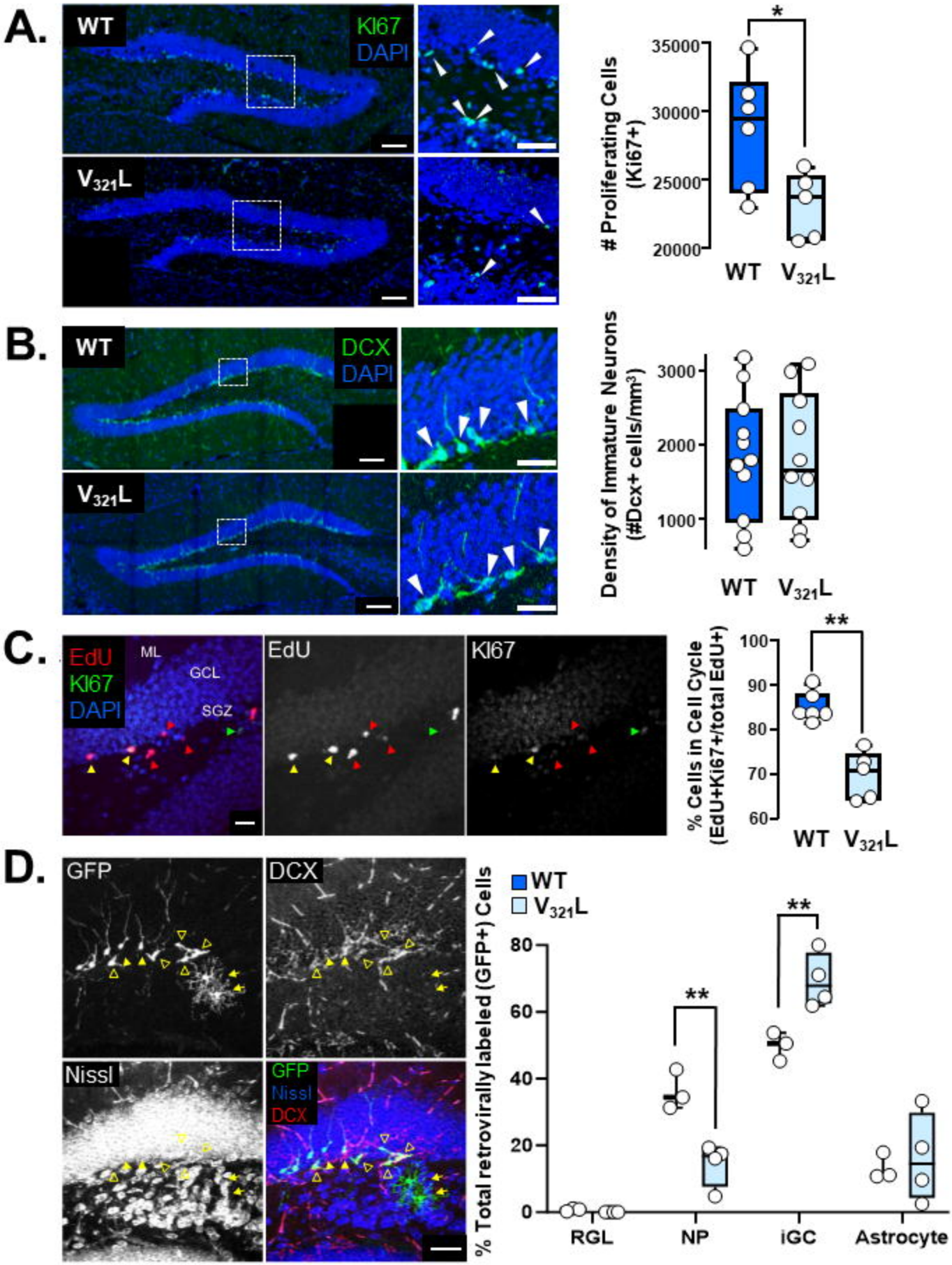
A.
WT
Ki67
DAPI
V321L
Proliferating Cells (Ki67+)
35000
30000
25000
20000
*
WT
V321L
B.
WT
DCX
DAPI
V321L
Density of Immature Neurons (#Dcx+ cells/mm3)
3000
2000
1000
WT
V321L
C.
EdU
Ki67
DAPI
ML
GCL
SGZ
EdU
Ki67
% Cells in Cell Cycle (EdU+Ki67+/total EdU+)
100
90
80
70
60
**
WT
V321L
D.
GFP
DCX
Nissl
GFP
Nissl
DCX
WT
V321L
% Total retrovirally labeled (GFP+) Cells
80
60
40
20
0
**
**
RGL
NP
iGC
Astrocyte

Figure 4

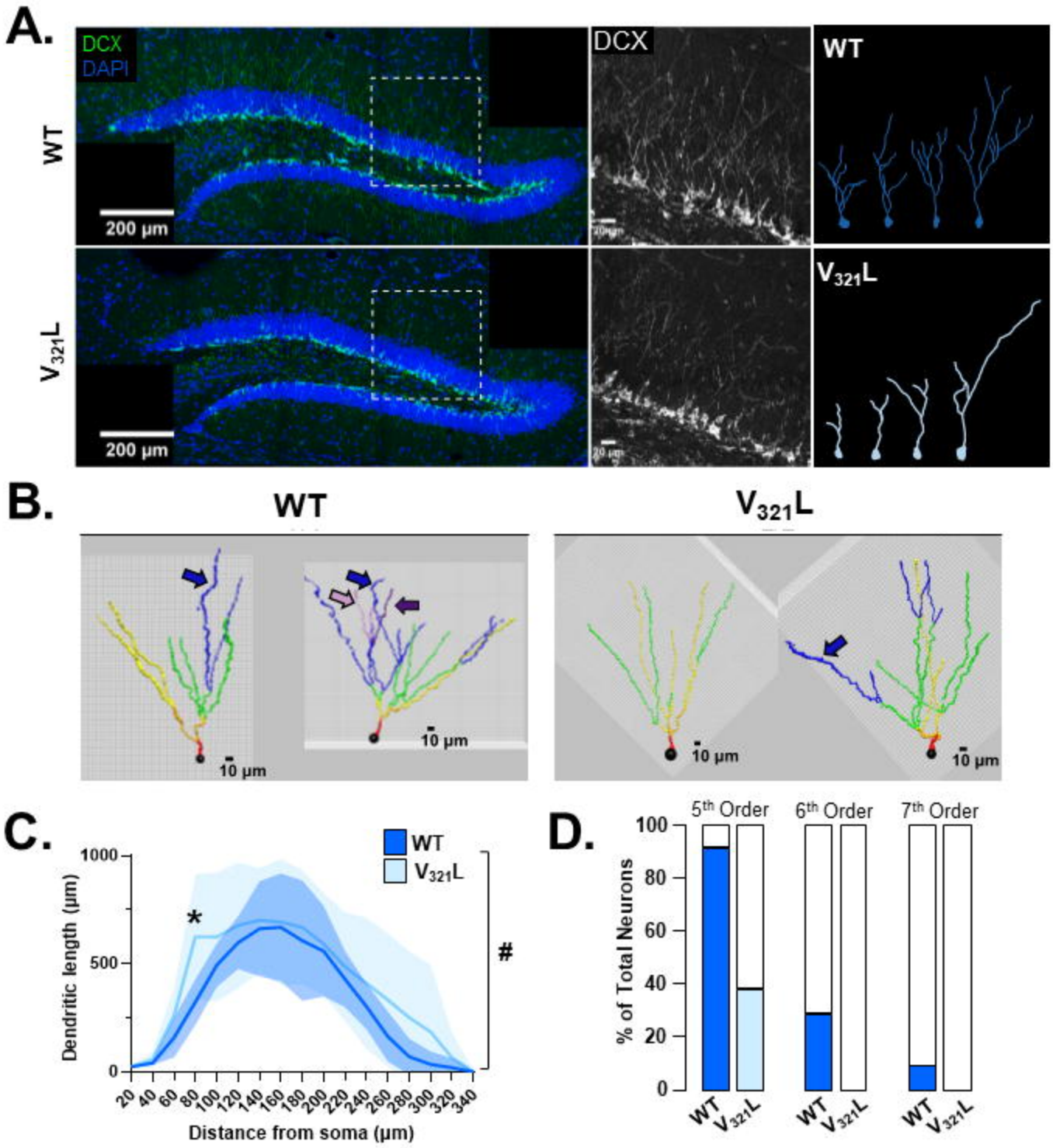
A.
DCX
DAPI
WT
200 µm
DCX
WT
V321L
200 µm
V321L
B.
WT
V321L
10 µm
10 µm
10 µm
10 µm
C.
WT
V321L
Dendritic length (µm)
1000
500
0
*
#
20 40 60 80 100 120 140 160 180 200 220 240 260 280 300 320 340
Distance from soma (µm)
D.
5th Order
6th Order
7th Order
% of Total Neurons
100
80
60
40
20
0
WT
V321L
WT
V321L
WT
V321L

Figure 5

A.

Enrichment Analysis (IPA)

↓

V321L vs. WT Schizophrenia-related DEGs (SCZ)

↓

With SCZ as seeds, grow network using remaining DEGs (SCZ+)

↓

Hub Gene Analysis (Mean Clique Clustering - MCC)

B.

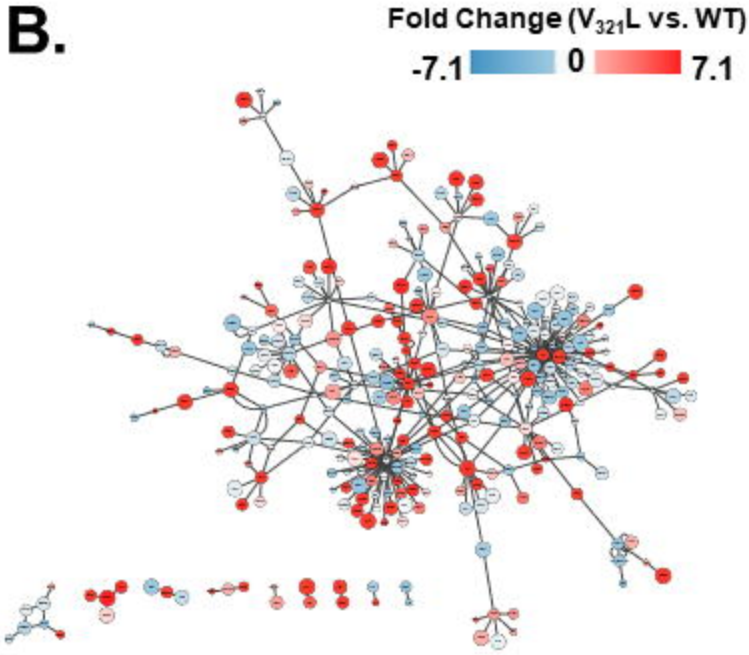

SCZ+ Network

C.

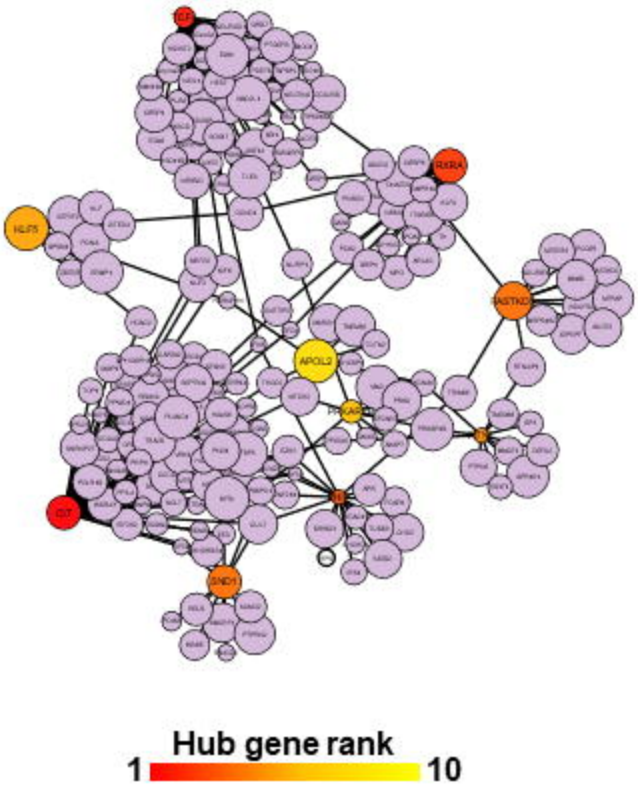

D.

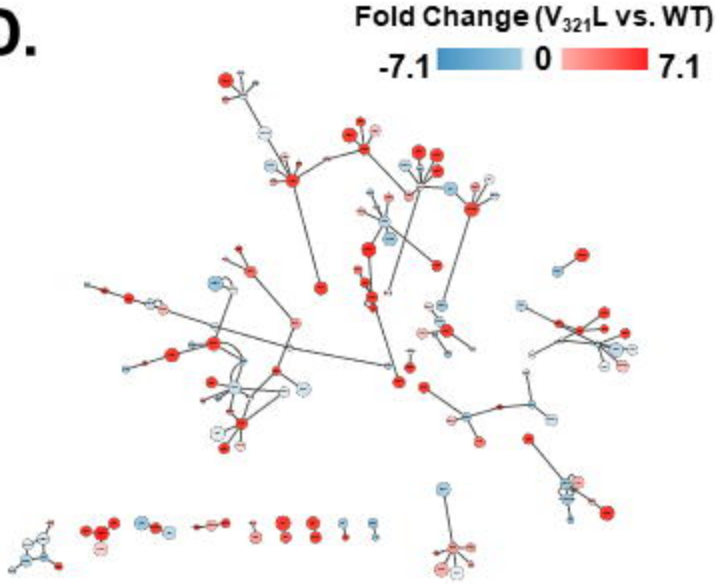

Hub-deleted SCZ+ Network

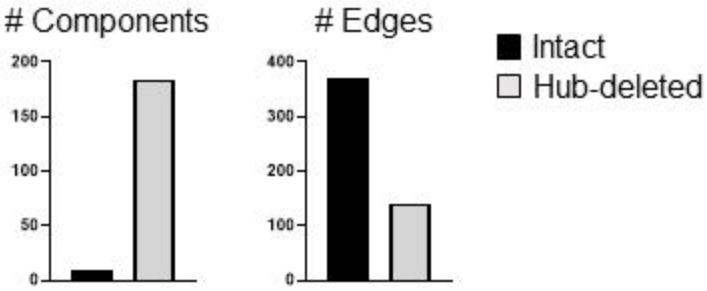

Figure 6

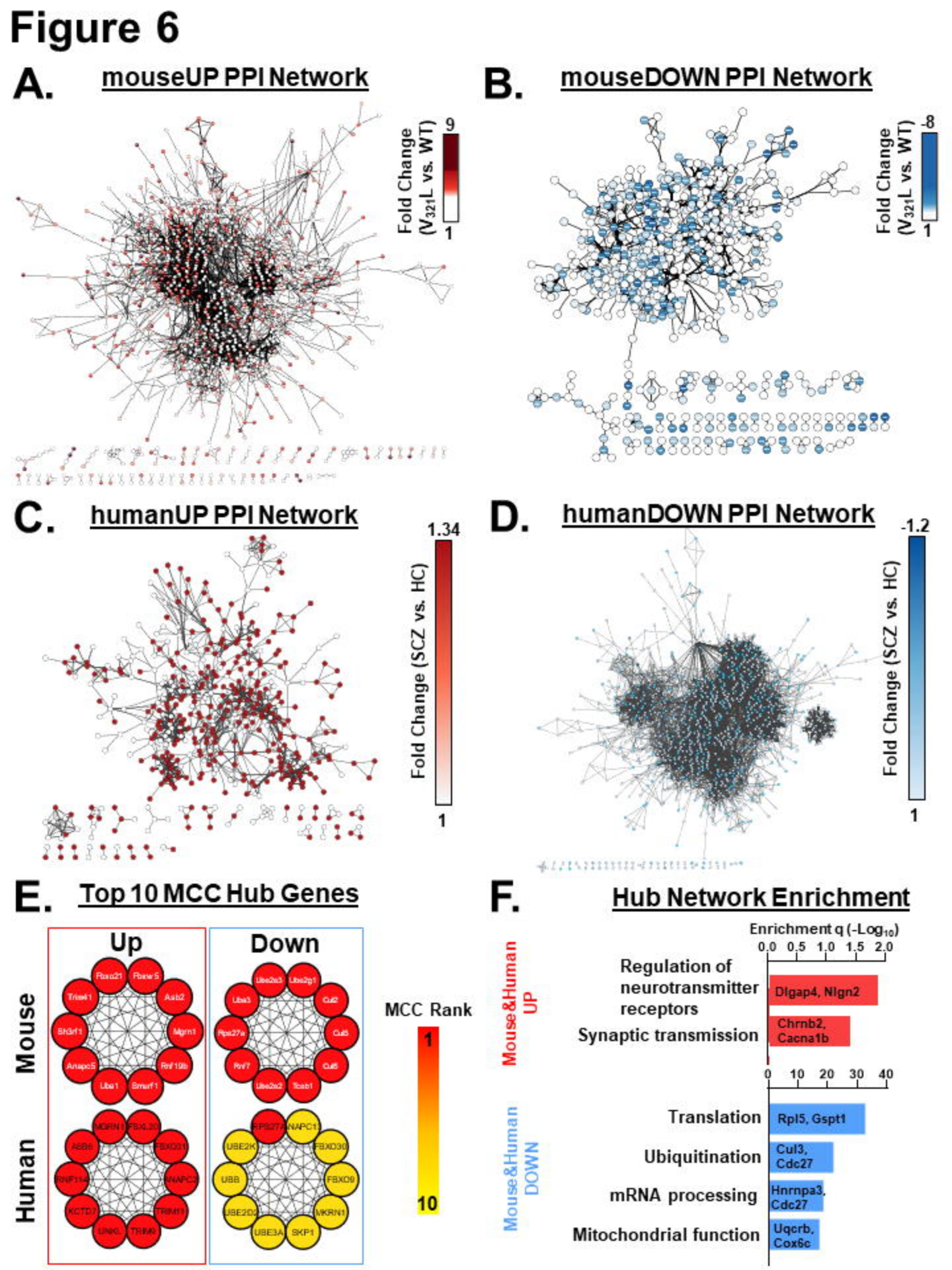

A.
mouseUP PPI Network
Fold Change ($V_{321}L$ vs. WT)
9
1
B.
mouseDOWN PPI Network
Fold Change ($V_{321}L$ vs. WT)
-8
1
C.
humanUP PPI Network
Fold Change (SCZ vs. HC)
1.34
1
D.
humanDOWN PPI Network
Fold Change (SCZ vs. HC)
-1.2
1
E.
Top 10 MCC Hub Genes
Up
Down
Mouse
Human
MCC Rank
1
10
F.
Hub Network Enrichment
Enrichment q (-Log10)
0.0 0.5 1.0 1.5 2.0
Mouse&Human UP
Regulation of neurotransmitter receptors
Dlgap4, Nlgn2
Synaptic transmission
Chrnb2, Cacna1b
0 10 20 30 40
Mouse&Human DOWN
Translation
Rpl5, Gspt1
Ubiquitination
Cul3, Cdc27
mRNA processing
Hnrnpa3, Cdc27
Mitochondrial function
Uqcrb, Cox6c